**TECHNISCHE
UNIVERSITÄT
DRESDEN**

Top quark background uncertainty and fake lepton background estimation in the search for a light CP-odd Higgs boson using the ATLAS detector

Master-Arbeit
zur Erlangung des Hochschulgrades
Master of Science
im Master-Studiengang Physik

vorgelegt von

Christian Schmidt
geboren am 27.03.1999 in Dresden.

Institut für Kern- und Teilchenphysik
Fakultät Physik
Bereich Mathematik und Naturwissenschaften
Technische Universität Dresden
2023

Eingereicht am 16.06.2023

Zusammenfassung

Diese Arbeit befasst sich mit Verbesserungen der Suche nach einem leichten, CP-ungeraden Higgs-Boson A. Dieses A-Boson wird von der Theorie des Zwei-Higgs-Dublett-Modells (2HDM) vorhergesagt, welches das Standardmodell um ein zusätzliches Higgs-Dublett erweitert. Die Suche fokussiert sich auf die Flavor-ausgerichtete Variante der Theorie (flavor-aligned 2HDM), in welcher die Yukawa-Kopplungen der beiden Dubletts für jeden Fermion-Typ proportional zueinander sind. Diese Theorie könnte die Diskrepanz zwischen experimentellen Messungen des anomalen magnetischen Moments des Myons und der Vorhersage des Standardmodells erklären.

In dem Signalprozess, auf welchen die Analyse ausgerichtet ist, wird ein A-Boson mit einer Masse zwischen $20\,\text{GeV}$ und $110\,\text{GeV}$ durch Gluon-Fusion erzeugt. Es zerfällt dabei in zwei Tau-Leptonen, welche weiter leptonisch in ein Elektron und ein Myon sowie zugehörige Neutrinos zerfallen. Die genutzten Daten wurden mit dem ATLAS-Detektor während Run-2 des Large Hadron Collider (LHC) gemessen. Sie stammen aus Proton-Proton-Kollisionen mit einer Schwerpunktsenergie von $13\,\text{TeV}$ und einer integrierten Luminosität von $140\,\text{fb}^{-1}$.

Die Analyse wurde gegenüber früheren Versionen weiter vervollständigt, indem die systematischen Unsicherheiten berechnet wurden, welche für Hintergrundprozesse mit zerfallenden Top-Quarks durch die Modellierung der Hintergründe mit Monte-Carlo-Generatoren entstehen. Weiterhin wurde mit der Matrix-Methode ein verbesserter Algorithmus implementiert, um den Hintergrund von Fake-Leptonen, die durch fehlidentifizierte Jets erzeugt werden, abzuschätzen.

Abstract

In this thesis, improvements in the search for a light CP-odd Higgs boson A are presented. The boson A is predicted by the two-Higgs doublet model (2HDM), which extends the Standard Model by an additional Higgs doublet. The search focuses on the flavor-aligned version of the 2HDM, in which the Yukawa couplings for the two doublets are proportional for each fermion type. This theory might explain the discrepancy between experimental measurements of the anomalous magnetic moment of the muon from the theoretical predictions of the Standard Model.

The analysis is sensitive to a signal process in which an A boson with a mass between $20\,\mathrm{GeV}$ and $110\,\mathrm{GeV}$ is produced via gluon fusion and decays into two tau leptons, which further decay into one electron and one muon together with associated neutrinos. It uses data produced from proton-proton collisions during Run 2 of the Large Hadron Collider (LHC) and recorded by the ATLAS detector, with a center-of-mass energy of $13\,\mathrm{TeV}$ and an integrated luminosity of $140\,\mathrm{fb}^{-1}$. The analysis is driven forward towards completion by calculating systematic uncertainties due to the Monte Carlo background modeling, specifically those related to the background from top quark decays. Additionally, the matrix method is implemented as an improved data-driven method to estimate the background due to fake leptons, caused by misidentified jets.

Contents

1 Introduction

The search for the fundamental constituents of matter has a long history, stretching back to atomic theory in ancient Greece. Yet it took until 1897 for the discovery of the electron as the first fundamental particle by J.J. Thomson [1], and until 1937 for the next elementary particle, the muon, to be found. Since then, the field of particle physics has progressed a lot, aided by the development of quantum electrodynamics (QED) as the first quantum field theory [2, 3].

In the 1950s, large numbers of hadronic particles were discovered in cloud chambers, and their organization into multiplets in 1961 by Y. Ne'eman and M. Gell-Mann [4, 5] led to the postulation of quarks as fundamental particles [6, 7]. This was later extended into a theory of quantum chromodynamics (QCD) to explain the strong interactions between quarks [8, 9].

In parallel to these developments, the theory of weak interactions by S.L. Glashow, A. Salam and S. Weinberg [10, 11] introduced the bosons $W^\pm$ and Z. This theory already required the weak gauge bosons to have mass, but could not explain the source of the masses. This problem was solved with the Higgs mechanism, which was formulated in 1964 by multiple groups [12–14] and applied to the non-abelian case of the weak interaction by T.W.B. Kibble in 1967 [15]. It introduces a scalar isospin doublet field with spontaneously broken symmetry, which couples to the weak gauge bosons to produce mass terms. One degree of freedom of this doublet becomes a physical field, corresponding to a massive Higgs boson with spin 0. The W and Z bosons were experimentally observed in 1983 at the Super Proton Synchrotron accelerator [16, 17], while the Higgs boson was finally found in 2012 at the Large Hadron Collider (LHC) [18, 19].

These theories of leptons, quarks, strong and electroweak interactions and the Higgs field combined form the Standard Model (SM) of particle physics. It represents our current understanding of fundamental particles and their interactions, with the exception of gravity, which is described by General Relativity [20]. To this date, the SM fits experimental observations exceptionally well. However, some phenomena hint at physics beyond the Standard Model: Astronomical observations imply the existence of dark matter, the violation of CP symmetry in the SM is too small to explain the origin of the matter-antimatter asymmetry in the universe, and the current experimental value of the anomalous magnetic moment of the muon deviates significantly from the theoretical prediction.

One possible extension of the SM is the two-Higgs doublet model (2HDM). It adds a second Higgs doublet to the theory, thereby predicting four additional Higgs bosons H, $H^\pm$ and A. For some values of the additional parameters for the second Higgs doublet, it is possible to explain the observed deviation of the anomalous magnetic moment of the muon while keeping the theory consistent with other experimental measurements. These

considerations point towards a low mass for the new CP-odd A boson and relatively large couplings of the A boson to both leptons and up-type quarks.

This thesis presents work on the search for the A boson with a cut-based analysis of data from the ATLAS detector. It builds on the theses of Paul Moder [21], Tom Kreße [22] and Xynia Sonntag [23], who started, extended and optimized the analysis. To make it ready for the unblinding procedure, systematic uncertainties due to Monte Carlo generator modeling are studied and an improved algorithm for fake lepton background estimation is implemented.

This work is structured as follows: Chapter 2 gives an overview of the Standard Model with a focus on the Higgs sector, and introduces the flavor-aligned 2HDM as the theoretical foundation of the analysis. Chapter 3 describes the setup of the ATLAS experiment as part of the LHC, which is the source of experimental data used in this thesis. In chapter 4, the operating principle of Monte Carlo event generators for the theoretical prediction of detector data is discussed. The analysis itself is the subject of chapter 5, which examines the relevant signal and background processes, discusses the analysis selection and background estimation, and presents my contributions. Expected results of the analysis in the form of exclusion limits are presented in chapter 6. Finally, chapter 7 summarizes the main points and results of this thesis and presents a look into the future of the analysis and beyond.

2 Theory

2.1 The Standard Model of particle physics

The Standard Model (SM) of particle physics is a quantum field theory describing elementary particles and their interactions. It includes all known elementary particles and is arguably the most well-tested theory in physics.

Of the four fundamental forces electromagnetism, weak and strong force, and gravity, the Standard Model describes the first three. At the scale where quantum mechanical effects play a role, the influence of gravity between individual particles is negligible. While external gravitational effects can be included by extending the Standard Model to curved spacetime, there is no generally accepted quantum theory including gravity to date.

The elementary particles of the Standard Model can be divided into *fermions* with half-integer spin and *bosons* with integer spin. The former include leptons and quarks, while the latter encompass the gauge bosons and the Higgs particle.

2.1.1 Fermions

The Standard Model contains twelve different elementary fermions, together with their antiparticles. They are divided into three generations of *quarks* and three generations of *leptons*. Each quark generation contains a doublet of one "up-type" and one "down-type" quark, and similarly every lepton generation contains one charged lepton and one corresponding *neutrino*. Fermions in different generations of the same type (up quark, down quark, charged lepton, neutrino) have the same charges, only different masses.

As all Fermions in the Standard Model have spin $\frac{1}{2}$, their fields can have both left-handed and right-handed components. Since parity is not conserved in the SM (and indeed is maximally violated by the weak interaction), these chiral components can have different charges. Quarks and charged leptons have Dirac mass terms, which couple left-handed and right-handed fields to each other.

For a long time neutrinos were thought to be massless, but since the observation of neutrino oscillations we know that they have very small nonzero masses. It is still unknown whether neutrinos have Majorana or Dirac masses, and whether right-handed neutrinos exist.

2.1.2 Forces and gauge bosons

The forces in the Standard Model are described by gauge symmetry with a total gauge group $SU(3)_C \times SU(2)_L \times U(1)_Y$. The factor $SU(3)_C$ represents the color charge symmetry

of the *strong interaction*, which is carried by the massless *gluons g* as the corresponding gauge bosons.

The electroweak gauge group $SU(2)_L \times U(1)_Y$ represents the symmetries of *weak isospin* I_W and *weak hypercharge* Y_W. This symmetry is spontaneously broken by the Higgs mechanism (see section 2.1.4). The electromagnetic subgroup $U(1)_Q$ is not affected by the symmetry breaking. The *weak gauge bosons* W^+, W^- and Z aquire a mass due to the Higgs mechanism, while the *photon γ* as the gauge boson coupling to electromagnetic charge Q remains massless.

The way the elementary particles interact through forces is determined by their transformation behavior under the gauge group. Their charges are given by the eigenvalues of the Lie algebra generators[1]. Every force only couples to particles which carry a nonzero charge associated with the corresponding gauge group, or equivalently to particles which transform under a nontrivial representation of the corresponding gauge group. Sets of particles which are closed under the group action are referred to as multiplets; gauge boson interactions can only convert particles into other particles from the same multiplet.

All quarks carry the color charge associated with the strong interaction, while leptons are color-neutral. At low energy scales, the coupling constant of the strong force diverges and the interaction becomes non-perturbative. As a result, quarks are only found as constituents of bound color-neutral states, the hadrons.

Up-type quarks carry an electrical charge of $Q = +2/3$ and down-type quarks have $Q = -1/3$. The electron, muon and tau are charged with $Q = -1$, while neutrinos are electrically neutral. The weak isospin I_W and weak hypercharge $Y = Q - I_W^3$ are different for left-handed and right-handed components, as explained in the following section.

The gauge bosons can also carry charges, they transform under the adjoint representation of their gauge group. Accordingly, gluons have a color charge, and $W^\pm$ bosons have $Q = I_W^3 = \pm 1$. Photons as carriers of the abelian $U(1)_Q$ are neutral.

2.1.3 Weak interaction

The kinetic term in the Langrangian for a fermion multiplet F has the form

$$\mathcal{L}_F = \bar{F}\, i\gamma^\mu D_\mu F \tag{2.1}$$

where D^μ is the gauge-covariant derivative, which introduces interaction terms with the relevant gauge fields.

For the weak interaction, the covariant derivative of a multiplet F is defined as

$$D^\mu F(x) = \partial^\mu F(x) + \sum_a ig_W W_a^\mu T_a F(x) + ig_Y B^\mu Y F(x) \tag{2.2}$$

Here, W_a and B are the gauge fields, g_W and g_Y are coupling constants, Y is the hypercharge of the multiplet and T_a are the generators of $SU(2)_L$.

---

[1]Note that the charge eigenstates are not necessarily the same as the mass eigenstates – they might be superpositions.

	Generation	1	2	3	I_W^3	Y	Q
Quarks	left-handed	u_L	c_L	t_L	$\frac{1}{2}$	$\frac{1}{6}$	$\frac{2}{3}$
		d_L	s_L	b_L	$-\frac{1}{2}$	$\frac{1}{6}$	$-\frac{1}{3}$
	right-handed	u_R	c_R	t_R	0	$\frac{2}{3}$	$\frac{2}{3}$
		d_R	s_R	b_R	0	$-\frac{1}{3}$	$-\frac{1}{3}$
Leptons	left-handed	ν_e	ν_μ	ν_τ	$\frac{1}{2}$	0	$-\frac{1}{2}$
		e_L	μ_L	τ_L	$-\frac{1}{2}$	-1	$-\frac{1}{2}$
	right-handed	e_R	μ_R	τ_R	0	-1	-1

Table 2.1: Electroweak charges of fermions in the Standard Model

The weak interaction acts differently on left-handed and right-handed fields. Left-handed fields form $\mathrm{SU}(2)_\mathrm{L}$-doublets

$$Q_\mathrm{L}^i = \begin{pmatrix} u_\mathrm{L}^i \\ d_\mathrm{L}^i \end{pmatrix} \quad \text{for quarks and} \quad L_\mathrm{L}^i = \begin{pmatrix} \nu_\mathrm{L}^i \\ l_\mathrm{L}^i \end{pmatrix} \quad \text{for leptons,} \tag{2.3}$$

while the right-handed fields u_R^i, d_R^i and l_R^i are singlets. For left-handed fermion doublets, the generators of $\mathrm{SU}(2)_\mathrm{L}$ have the form $T_a = \frac{1}{2}\sigma_a$ with the Pauli matrices

$$\sigma_1 = \begin{pmatrix} 0 & 1 \\ 1 & 0 \end{pmatrix}, \quad \sigma_2 = \begin{pmatrix} 0 & -i \\ i & 0 \end{pmatrix}, \quad \sigma_3 = \begin{pmatrix} 1 & 0 \\ 0 & -1 \end{pmatrix} \tag{2.4}$$

while for singlets $T_a = 0$. The weak charge eigenvalues for fermions are listed in table 2.1.

The gauge fields W_1, W_2, W_3 and B aquire non-diagonal mass terms through the Higgs mechanism (see section 2.1.4). The mass (and electric charge) eigenstates $W^\pm$, Z and γ are related to the original fields by

$$W^\pm = \frac{1}{\sqrt{2}}(W_1 \pm i\,W_2) \tag{2.5}$$

$$\begin{pmatrix} \gamma \\ Z \end{pmatrix} = \begin{pmatrix} \cos\theta_W & \sin\theta_W \\ -\sin\theta_W & \cos\theta_W \end{pmatrix} \begin{pmatrix} B \\ W_3 \end{pmatrix} \tag{2.6}$$

The weak mixing angle θ_W is a function of the two coupling constants:

$$\tan\theta_W = \frac{g_Y}{g_W}. \tag{2.7}$$

The photon field γ couples with strength

$$e = g_W \sin\theta_W \tag{2.8}$$

to the electric charge Q, which is related to I_W^3 and Y by the Gell-Mann-Nishijima relation

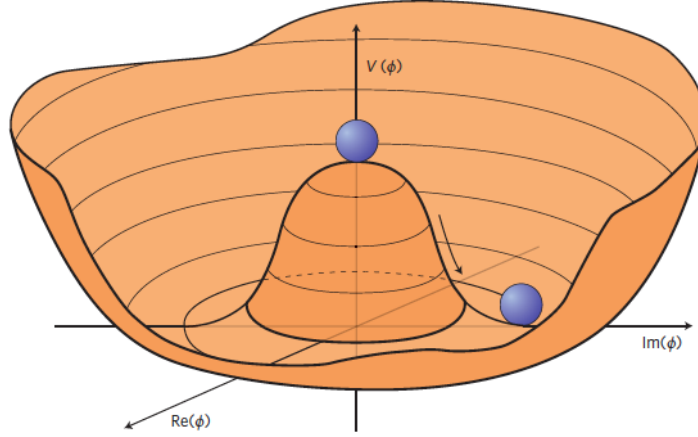$$Q = I_W^3 + Y. \tag{2.9}$$

2.1.4 Higgs mechanism

Figure 2.1: Simplified illustration of the shape of the Higgs potential, with symmetric stationary point and symmetry-breaking vacuum. [24]

A gauge theory like the SM cannot have explicit mass terms for the gauge bosons in the Lagrangian, because they are not invariant under gauge transformations. Additionally, $SU(2)_L$ acting differently on left-handed and right-handed doublets is incompatible with normal Dirac mass terms $m\bar{\psi}\psi = m\psi_L\psi_R$ for fermions. These considerations lead to the Higgs mechanism, which introduces a new scalar field to solve both problems.

The Higgs field is an isospin doublet

$$\phi = \begin{pmatrix} \phi^+ \\ \phi^0 \end{pmatrix} \tag{2.10}$$

with complex components ϕ^+ and ϕ^0, so it has four degrees of freedom. Its weak hypercharge is $Y = 1$. The Lagrange density for this field is

$$\mathcal{L}_H = (D_\mu \phi)^\dagger (D^\mu \phi) - V_H(\phi) \tag{2.11}$$

with the $SU(2)_L$-symmetric Higgs potential

$$V_H(\phi) = -\mu^2 \phi^\dagger \phi + \lambda (\phi^\dagger \phi)^2. \tag{2.12}$$

Here μ and λ are positive real parameters.

The term $-\mu^2 \phi^\dagger \phi$ has the form of a mass term, but with opposite sign. Consequently,

the symmetric stationary point of the potential at $\phi = 0$ is not a minimum. Rather, the potential has a "mexican hat" shape with degenerate minima at

$$\phi^\dagger \phi = \frac{\mu^2}{2\lambda} = \frac{v^2}{2}, \tag{2.13}$$

as illustrated in figure 2.1. Choosing one of them as the vacuum spontaneously breaks the SU(2) symmetry of the potential.

Since the Higgs field transforms under the $\mathrm{SU(2)_L}$ gauge group, fields with the same absolute value $\phi^\dagger \phi$ can be transposed into each other with a gauge transformation. It is always possible to fix a gauge to make the upper component of ϕ zero and the lower component real, such that

$$\phi(x) = \frac{1}{\sqrt{2}} \begin{pmatrix} 0 \\ v + h(x) \end{pmatrix} \tag{2.14}$$

with the vacuum expectation value $v = \sqrt{\mu^2/\lambda}$. Expanding the terms of the Higgs Lagrangian using this gauge yields

$$\mathcal{L}_H = (\partial_\mu \phi)^\dagger (\partial^\mu \phi) - \phi^\dagger \phi \left(\left| \tfrac{1}{2} g_W W_1^\mu \right|^2 + \left| \tfrac{1}{2} g_W W_2^\mu \right|^2 + \left| \tfrac{1}{2} g_W W_3^\mu + \tfrac{1}{2} g_Y B^\mu \right|^2 \right) - V_H$$

$$= (\partial_\mu \phi)^\dagger (\partial^\mu \phi) - \frac{v^2}{8} \left(1 + \frac{h}{v} \right)^2 \left(g_W^2 W_\mu^+ W^{+\mu} + g_W^2 W_\mu^- W^{-\mu} + \left(g_W^2 + g_Y^2 \right) Z_\mu Z^\mu \right)$$

$$- \mu^2 h^2(x) - \lambda v h^3(x) - \tfrac{1}{4} \lambda h^4(x) + \text{const.} \tag{2.15}$$

The quadratic terms produce the masses

$$m_W = \tfrac{1}{2} v\, g_W \tag{2.16}$$

$$m_Z = \tfrac{1}{2} v \sqrt{g_W^2 + g_Y^2} = \tfrac{1}{2} v\, g_W \sec \theta_W \tag{2.17}$$

$$m_H = \mu = \sqrt{2\lambda}\, v \tag{2.18}$$

while the photon has no associated mass term, so $m_A = 0$.

If the Higgs field did not interact with the weak force (i.e. did not have a covariant derivative in the Lagrangian), the spontaneous symmetry breaking of the continuous global SU(2) symmetry would make the three degrees of freedom of ϕ orthogonal to its vacuum expectation become massless Goldstone modes. In this scenario, with the weak force not influenced by the Higgs, the gauge freedom would remove the longitudinal degrees of freedom from the three massless W gauge bosons. With the Higgs mechanism, the gauge freedom instead eliminates the Goldstone modes of the Higgs (see eq. 2.14), while the gauge bosons acquire mass and keep their longitudinal polarization modes.

The nonzero vacuum expectation value of the Higgs field also allows for an explanation

of the fermion masses by introducing *Yukawa couplings*:

$$\mathcal{L}_Y = -\sum_{ij} Y_l^{ij} \, \bar{L}_{\mathrm{L}}^i \phi \, l_{\mathrm{R}}^j + Y_d^{ij} \, \bar{Q}_{\mathrm{L}}^i \phi \, d_{\mathrm{R}}^j + Y_u^{ij} \, \bar{Q}_{\mathrm{L}}^i \phi^c \, u_{\mathrm{R}}^j + \text{h.c.} \tag{2.19}$$

where $\bar{L}_{\mathrm{L}}$ and $\bar{Q}_{\mathrm{L}}$ are the left-handed lepton and quark doublets; l_{R}, d_{R} and u_{R} are the right-handed charged lepton, down-type quark and up-type quark fields, respectively; i and j are flavor indices; $\phi^c = i\sigma_3\phi^*$ is the charge conjugate; and Y_l, Y_d and Y_u are complex coupling matrices. Mass eigenstates correspond to eigenvalues of the coupling matrices, with masses related to the eigenvalues y by

$$m = \frac{v}{\sqrt{2}} \, y. \tag{2.20}$$

2.1.5 Discrete symmetries

In the context of quantum field theories like the SM, there are three important discrete symmetry operations related to the symmetries of the surrounding spacetime.

The parity operator P mirrors all spatial coordinates, the time reversal operator T inverts the direction of time evolution, and the charge conjugation operator C converts every particle into its antiparticle, therefore flipping the sign of every charge:

$$P \, \psi(x,y,z,t) = \psi(-x,-y,-z,t) \tag{2.21}$$

$$T \, \psi(x,y,z,t) = \psi(x,y,z,-t) \tag{2.22}$$

$$C \, \psi(x,y,z,t) = \bar{\psi}(x,y,z,t) \tag{2.23}$$

For each operator, applying it twice returns the original state[2], so $P^2 = T^2 = C^2 = 1$. As a result the eigenvalues can only be $+1$ or -1.

Parity as the $\mathbb{Z}_2$ subgroup of the spatial O(3) symmetry is related to the spin of a particle. Fermions with spin $1/2$ have a parity of $+1$ and antifermions have parity -1. Bosons with spin 0 can be scalar with parity $+1$ or pseudoscalar with parity -1; similarly spin-1 particles with parity $-1/+1$ are called vector bosons and pseudovector bosons, respectively.

The strong and electromagnetic interactions are invariant under parity. They act equally on left-handed and right-handed fields. However, the weak interaction only couples to left-handed particles and right-handed antiparticles, which maximally breaks the conservation of parity.

Combining a parity transform with charge conjugation results in the CP symmetry operation, which turns left-handed particles into right-handed antiparticles and vice versa. At first glance, adding charge conjugation seems to restore the symmetry of the weak interaction, but CP is not an exact symmetry of the Standard Model: The CKM matrix, which relates the charge eigenstates of the weak isospin to the mass eigenstates of the

---

[2]In general, the squared operators can also apply a global phase change, with the phase only depending on globally conserved quantities. In the SM, all conserved quantities are from continuous symmetries, so the C, P and T operators can be redefined to have square 1. [25]

quarks, contains a complex phase, breaking CP invariance.

The combination CPT of all three operations – simultaneously inverting space, time and charge – is a fundamental symmetry for which no violation has been observed. The CPT theorem states that this symmetry has to be exact in the context of Lorentz-invariant local causal quantum field theories. [26]

2.2 Two-Higgs doublet model

The Two-Higgs doublet model (2HDM) is one of the simplest possible extensions of the Standard Model. Instead of the single Higgs doublet, it introduces two independent scalar doublets

$$\phi_1 = \begin{pmatrix} \phi_1^+ \\ \phi_1^0 \end{pmatrix}, \quad \phi_2 = \begin{pmatrix} \phi_2^+ \\ \phi_2^0 \end{pmatrix} \tag{2.24}$$

without modifying the fermion and gauge sectors.

Adding this second doublet allows the model to explain phenomena such as the deviation of the anomalous magnetic moment oft the muon, or the baryon asymmetry in the universe [27, 28].

Supersymmetry also requires the existence of two Higgs doublets (together with supersymmetric partners). Normally a single Higgs doublet can couple to all fermions, and its non-zero vacuum expectation value produces mass terms for all of them. In a supersymmetric theory, however, some of the Yukawa interaction terms from the ordinary theory would violate supersymmetry. As a result, every Higgs doublet can only produce mass terms for quarks of a given charge. To explain the masses of both up-type and down-type quarks, it is necessary to include at least two Higgs doublets in a supersymmetric theory. [29] This result also implies that supersymmetry requires a specific version of the 2HDM, in which down-type quarks couple to a different Higgs doublet compared to up-type quarks. The Minimal Supersymmetric Standard Model therefore uses the *Type II* 2HDM, as defined in table 2.2.

In general, the 2HDM can introduce new sources of CP symmetry violations, through CP-violating vacuum expectation values and/or Yukawa couplings. In the following we will exclude such models and assume that there is no CP violation in the scalar sector.

2.2.1 Higgs potential and physical fields

The potential for the two doublets is

$$\begin{aligned} V_H =& m_{11}^2 \phi_1^\dagger \phi_1 + m_{22}^2 \phi_2^\dagger \phi_2 - \{m_{12}^2 \phi_1^\dagger \phi_2 + \text{h.c.}\} \\ &+ \tfrac{1}{2}\lambda_1 (\phi_1^\dagger \phi_1)^2 + \tfrac{1}{2}\lambda_2 (\phi_2^\dagger \phi_2)^2 + \lambda_3 (\phi_1^\dagger \phi_1)(\phi_2^\dagger \phi_2) + \lambda_4 (\phi_1^\dagger \phi_2)(\phi_2^\dagger \phi_1) \\ &+ \{\tfrac{1}{2}\lambda_5 (\phi_1^\dagger \phi_2)^2 + \lambda_6 (\phi_1^\dagger \phi_1)(\phi_1^\dagger \phi_2) + \lambda_7 (\phi_2^\dagger \phi_2)(\phi_1^\dagger \phi_2) + \text{h.c.}\} \end{aligned} \tag{2.25}$$

with real parameters m_{ij} and λ_i, which has a minimum at[3]

$$\langle \phi_1 \rangle = \frac{1}{\sqrt{2}} \begin{pmatrix} 0 \\ v_1 \end{pmatrix}, \quad \langle \phi_2 \rangle = \frac{1}{\sqrt{2}} \begin{pmatrix} 0 \\ v_2 \end{pmatrix} \tag{2.26}$$

with the VEVs v_1 and v_2. Their ratio is ususally denoted by

$$\tan \beta = \frac{v_2}{v_1}. \tag{2.27}$$

We can apply a basis rotation to the two doublets to redefine them as

$$\begin{pmatrix} \Phi_1 \\ \Phi_2 \end{pmatrix} = \begin{pmatrix} \cos \beta & \sin \beta \\ -\sin \beta & \cos \beta \end{pmatrix} \tag{2.28}$$

so that Φ_2 has the VEV zero and Φ_1 has VEV $v = \sqrt{v_1^2 + v_2^2}$. In this "Higgs basis", after choosing a suitable gauge, the doublets have the form

$$\Phi_1(x) = \frac{1}{\sqrt{2}} \begin{pmatrix} 0 \\ v + \rho_1(x) \end{pmatrix} \quad \text{and} \quad \Phi_2 = \frac{1}{\sqrt{2}} \begin{pmatrix} H^+(x) + iH^-(x) \\ \rho_2(x) + iA(x) \end{pmatrix} \tag{2.29}$$

where ρ_1 and ρ_2 mix to form the scalar fields of the lighter h and heavier H bosons, H^+ and H^- represent charged Higgs bosons, and A corresponds to a pseudoscalar CP-odd boson. [30]

2.2.2 Flavor-aligned 2HDM

Model		Type I	Type II	Type X	Type Y
Coupling doublet	up-type quark	ϕ_2	ϕ_2	ϕ_2	ϕ_2
	down-type quark	ϕ_2	ϕ_1	ϕ_2	ϕ_1
	charged lepton	ϕ_2	ϕ_1	ϕ_1	ϕ_2
Yukawa parameters	ζ_u	$\cot \beta$	$\cot \beta$	$\cot \beta$	$\cot \beta$
	ζ_d	$\cot \beta$	$-\tan \beta$	$\cot \beta$	$-\tan \beta$
	ζ_l	$\cot \beta$	$-\tan \beta$	$-\tan \beta$	$\cot \beta$

Table 2.2: Coupling doublets for the lepton types in the $\mathbb{Z}_2$-symmetric models, and the corresponding Yukawa parameters in the aligned 2HDM. [31]

In the Standard Model, the Yukawa couplings alone produce the fermion masses, so the Higgs couplings to the fermions are automatically diagonal in the fermion flavors. In the 2HDM, both doublets contribute mass terms, so there is no reason for the individual

---

[3]While for one doublet it is always possible to make the vacuum expectation neutral (upper component zero) and real, for two doublets charge-breaking and CP-breaking vacua would be possible. Here we simply assume that the vacuum expectation values do not have a relative phase and can be simultaneously rendered neutral and real.

couplings to be diagonal in the mass basis. This introduces *flavor-changing neutral currents* (FCNCs) into the theory. Experiments have established strong limits on the rate of FCNC interactions, using e.g. meson-antimeson mixing. This rules out most of the parameter space for the general 2HDM.

here are several ways to define Two-Higgs-doublet models which do not imply the existence of FCNCs at tree level, and thus remain phenomenologically viable.

The first approach is based on the Paschos-Glashow-Weinberg theorem [32], which implies that if each type of fermion (up-/down-type quark and charged lepton) only couples to a single Higgs doublet, neutral currents conserve flavor at tree level. In fact, this condition is the only way to exclude FCNCs *naturally*, i.e. for the entire parameter space. It can be imposed by a discrete $\mathbb{Z}_2$ symmetry acting on the (original, non-rotated) Higgs doublets as $\phi_1 \rightarrow -\phi_1, \ \phi_2 \rightarrow \phi_2$.

In the 2HDM, considering all cases of which doublet each type of fermion couples to leads to four types, see table 2.2. Without loss of generality, ϕ_2 is conventionally chosen to be the doublet which up-type quarks couple to. Each case corresponds to a specific transformation behavior of the fermion types under the $\mathbb{Z}_2$ symmetry, such that each fermion has the same behavior as the doublet it couples to.

As a second approach, tree-level FCNCs can be more generally excluded if the Yukawa coupling matrices for the two doublets are *aligned* in flavor space [33]. This means that for each type of fermion, the Yukawa couplings to the two doublets are proportional to each other. This property is conserved under a change to the Higgs basis. The proportionality constants can be different for up-type quarks, down-type quarks and charged leptons; they are denoted as ζ_u, ζ_d and ζ_l respectively. The $\mathbb{Z}_2$-symmetric models can be considered as special cases with specific values of $\zeta_{u,d,l}$, as indicated in table 2.2.

2.2.3 Contribution to anomalous magnetic moment of the muon

The muon as a spin-1/2 particle has an intrinsic magnetic moment

$$\mu = g_\mu \frac{e\hbar}{4m_\mu}. \tag{2.30}$$

The Dirac equation predicts a g-factor $g = 2$. Due to loop corrections, the true value is different, and the deviation is quantified by the anomalous magnetic moment

$$a_\mu = \frac{g_\mu - 2}{2}. \tag{2.31}$$

Experiments at Brookhaven National Laboratory (BNL) [35] and Fermi National Accelerator Laboratory (FNAL) [36] have measured an average value of

$$a_\mu^{\mathrm{Exp}} = 116\,592\,061(41) \times 10^{-11} \tag{2.32}$$

which deviates from the Standard Model prediction by

$$a_\mu^{\mathrm{Exp}} - a_\mu^{\mathrm{SM}} = 251(59) \times 10^{-11} \tag{2.33}$$
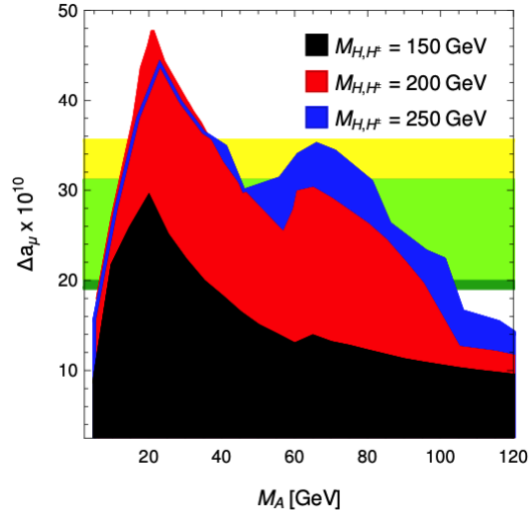
11

Figure 2.2: Maximum possible values of the deviation of the anomalous magnetic moment of the muon in the flavor-aligned Two-Higgs doublet model, as a function of the A boson mass for several values of $M_H = M_{H^\pm}$. The green band shows the 1σ region around the average experimental measurement. [34]

with a statistical significance of 4.2σ.

The flavor-aligned Two-Higgs doublet model offers a way to explain this deviation, because it introduces new loop diagrams involving the additional Higgs bosons as contributions to a_μ [34]. The 2HDM allows for a significant impact on the anomalous magnetic moment of the muon mostly in the parameter region where the A boson mass M_A is small and the Yukawa coupling parameters ζ_l and ζ_u are large [37, 38].

Taking into account the parameter constraints from the following section, one can calculate the maximum deviation of a_μ which the flavor-aligned 2HDM can explain, plotted in figure 2.2. The explainable region overlaps with the observed value for A boson masses between about $5\,\mathrm{GeV}$ and $100\,\mathrm{GeV}$.

2.2.4 Parameter constraints

Since the additional Higgs doublet also has an influence on other measurable quantities for which current results agree with the standard model prediction, the parameters of the 2HDM are constrained by various particle decay and collision measurements.

The lepton coupling parameter ζ_l has the weakest constraints: Its absolute value can be up to about 100, depending on the Higgs masses (see fig. 2.3). For A boson masses above $20\,\mathrm{GeV}$, the constraints arise from measurements of the decay $\tau \to \mu\nu_\tau\bar{\nu}_\mu$ and of leptonic Z boson decays. Below $20\,\mathrm{GeV}$, the process $ee \to \tau\tau(A) \to \tau\tau(\tau\tau)$ at the Large Electron-Positron Collider (LEP) more strongly constrains the value of ζ_l.

The coupling ζ_u to up-type quarks is constrained both by decays of hadrons containing bottom quarks (B physics) and LHC collision processes involving a new neutral Higgs
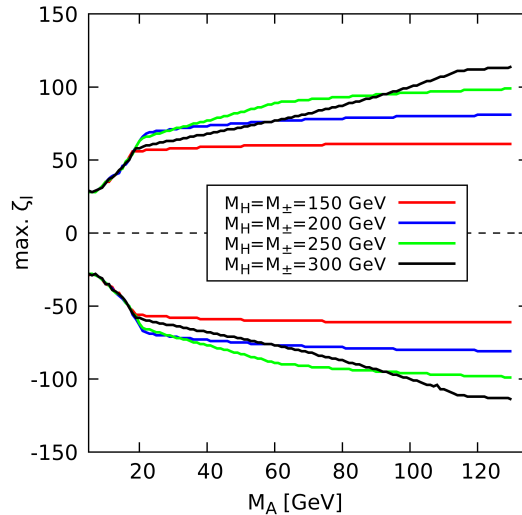
Figure 2.3: Maximum and minimum allowed values of the lepton Yukawa parameter ζ_l, as a function of the A boson mass for several values of $M_H = M_{H^\pm}$. [31]

boson (A or H) as an intermediate state. The resulting limits are shown in figure 2.4.

The most important B physics processes are $B_s \to \mu^+\mu^-$ and $b \to s\gamma$, which constrain ζ_u to below around 0.5. The impact of the LHC processes $pp \to A \to \tau\tau$ (which is also the subject of this analysis), $pp \to H \to \tau\tau$ (where H is the additional non-SM-like neutral Higgs) and of SM Higgs decays depends strongly on the mass of the A boson. For $M_A > M_Z$, the A boson decay produces τ pairs with an invariant mass above M_Z, which results in a strong constraint. In the case of a lower A mass, the H boson intermediate state is relevant. The constraints can be weaker if $H \to AA$ instead of $H \to \tau\tau$ is the dominant decay mode, which requires $M_A < \frac{1}{2}M_H$. If the A boson has a mass below $63\,\text{GeV}$, the SM Higgs can similarly decay to a pair of A bosons. From Higgs decay measurements we know this is very unlikely, which also constrains the probability of $H \to AA$ leading to stronger ζ_u limits.

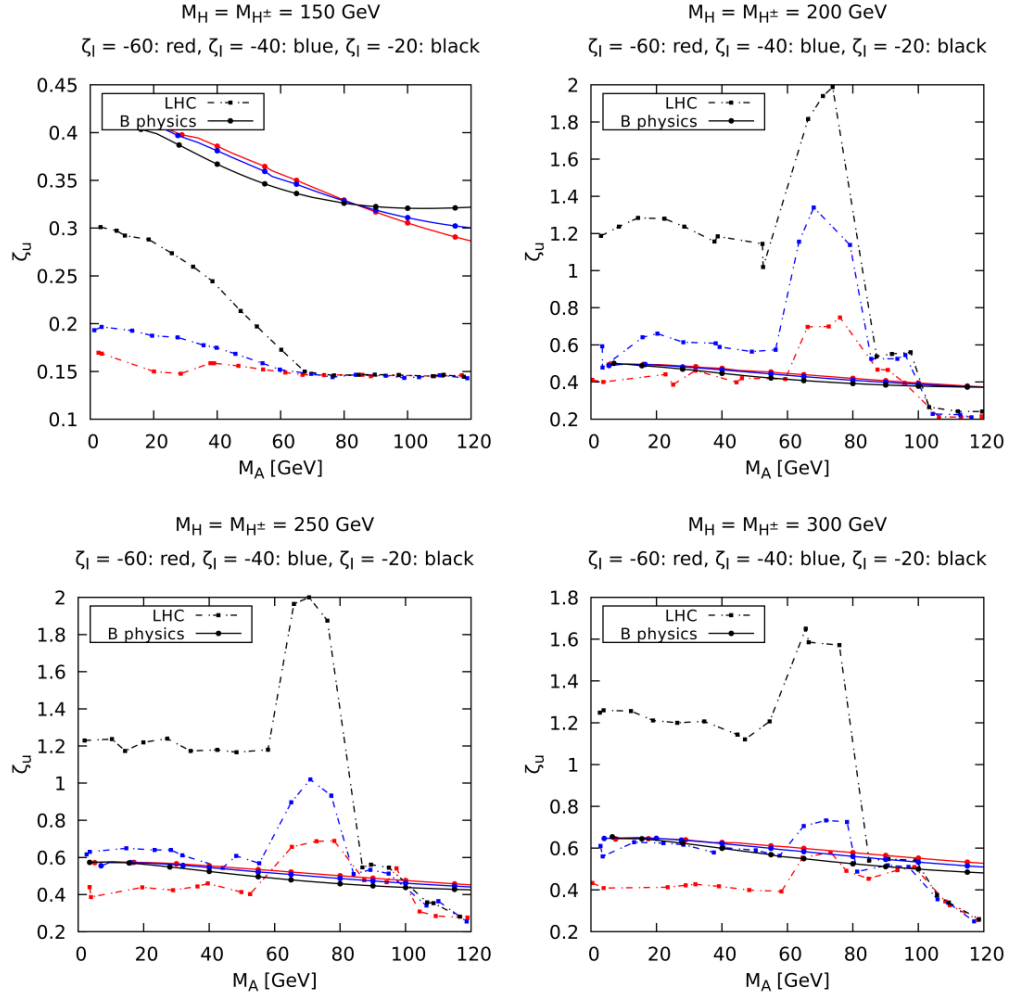A full discussion of the available parameter space can be found in [31].

Figure 2.4: Maximum allowed values of the up quark Yukawa parameter ζ_u as a function of the A boson mass, for different values of M_H, $M_{H^\pm}$ and ζ_l. The limits from B-physics (continuous lines) and LHC Higgs physics (dashed lines) are plotted separately. [31]

14

3 The LHC and ATLAS detector

3.1 The LHC accelerator

The LHC [39] is a ring accelerator designed for hadron-hadron collisions, and is part of the European Organization for Nuclear Research (CERN) accelerator complex as shown in figure 3.1. It is located in a 26.7 km long circular tunnel, which was originally built for the Large Electron-Positron Collider (LEP). The tunnel contains two parallel beamlines, one for each direction of the proton beam.
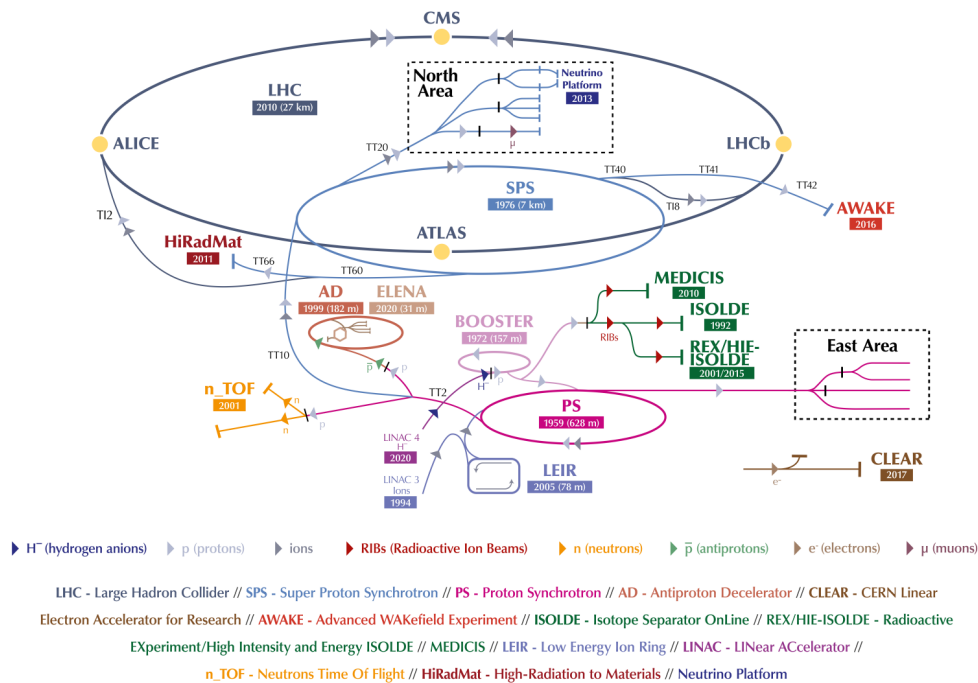

Figure 3.1: Schematic layout of the CERN accelerator complex. [40]

The beamlines are divided into eight circular arcs and eight straight segments. In the curved segments, superconducting dipole magnets keep the particles on their path, while quadrupole and higher dipole magnets keep the beam focused. Four of the straight segments accommodate RF cavities to accelerate the particles, collimators to clean the beam, and kicker magnets to divert the particles into dump blocks after operation or in an emergency. On the four other straight segments, the two beamlines cross within the detectors for the four largest LHC experiments: ATLAS [41], CMS [42], ALICE [43]

15

and LHCb [44]. The two high-luminosity experiments ATLAS and CMS are optimized for taking general-purpose collision data, which is used e.g. in analyses on Higgs physics, supersymmetry and CP violation. The LHCb experiment is focused on B-physics, while ALICE is used to investigate ion-ion collisions.

During proton mode operation, bunches of protons are created and pre-accelerated in the Super Proton Synchrotron complex (PSB, PS and SPS, see fig. 3.1). They are injected into the LHC at an energy of $450\,\mathrm{GeV}$ and further accelerated by the RF cavities. The protons circulate in opposite directions within the two adjacent beamlines, until they collide at one of the interaction points or are diverted into a dump block.

The data used in this analysis was produced during Run 2 [45], which took place between 2015 and 2018. During that time, each proton reached an energy of $6.5\,\mathrm{TeV}$, resulting in a total collision energy of $\sqrt{s} = 13\,\mathrm{TeV}$. Over the three years, the LHC achieved an integrated luminosity of $L_i = 140\,\mathrm{fb}^{-1}$, as shown in figure 3.2 [46]. This means that a process with cross section σ occurs in the data on average

$$N = \sigma\, L_i \tag{3.1}$$

times. The full definition for luminosity is given below in section 3.2.1.
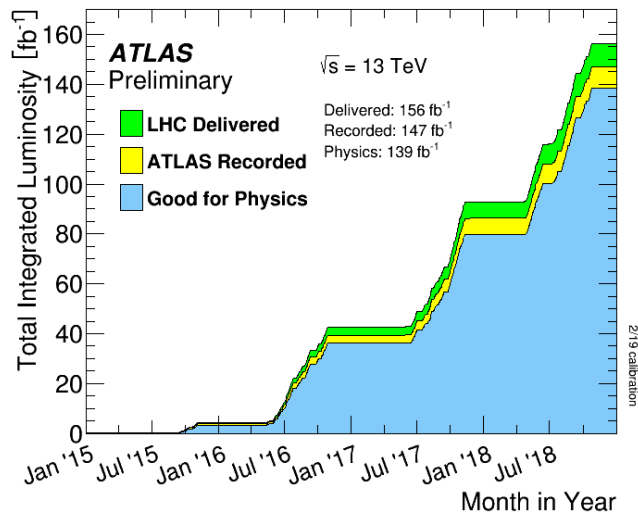

Figure 3.2: Cumulative luminosity over time recorded by the ATLAS detector during Run. [47] The graph uses the older luminosity estimate of $139\,\mathrm{fb}^{-1}$, which was revised to $140\,\mathrm{fb}^{-1}$ in 2022. [46]

In July 2022, the collider started its third run [48], with a collision energy of $13.6\,\mathrm{TeV}$. While Run 2 reached a peak instantaneous luminosity of $2.1 \times 10^{34}\,\mathrm{cm}^{-2}\mathrm{s}^{-1}$, Run 3 will reach a luminosity of $3 \times 10^{34}\,\mathrm{cm}^{-2}\mathrm{s}^{-1}$.

16

3.2 Collider phenomenology and definitions

3.2.1 Cross-section and luminosity

The *cross section* σ of a process is a measure of the probability of its occurrence. It is measured in Barn, where $1\,\mathrm{b} = 1 \times 10^{-28}\,\mathrm{m}^2$. For an idealized experiment in which incoming particles, distributed over an area A, interact with a single target, a process with cross section σ will occur with probability

$$p = \frac{\sigma}{A} \tag{3.2}$$

for each (randomly chosen) incoming particle.

In a collider, the rate at which interactions between the beam particles happen is measured by the *luminosity* L. If a process with cross section σ occurs at a rate $\dot{N}$, the luminosity is calculated as

$$L = \frac{\dot{N}}{\sigma}. \tag{3.3}$$

The integrated luminosity over a given time period is defined as

$$L_i = \int L \, \mathrm{d}x \tag{3.4}$$

such that the mentioned process occurs on average $\sigma \cdot L_i$ times within that period.

3.2.2 Detector coordinate system

Positions and directions in a detector are typically measured with respect to an orthonormal coordinate system, such that the z direction is parallel to the beam axis. For the ATLAS detector, the x-axis points towards the center of the LHC, the y-axis points upwards, and the direction of the z-axis is defined to complete the right-handed orthonormal system. [41]

Since the setup has rotational symmetry around the beam axis, it makes sense to also use spherical coordinates with a polar angle θ measured relative to the z-direction and an azimuthal angle ϕ measured counterclockwise from the x-axis.

Derived from the polar angle one can define the *pseudorapidity*

$$\eta = -\ln(\tan(\theta/2)), \tag{3.5}$$

which is useful because for ultrarelativistic particles ($v \approx c$), a difference in pseudorapidity $\Delta\eta$ is invariant under Lorentz boosts along the beam axis. As a measure of distance between particle directions in the collider one additionally defines

$$\Delta R = \sqrt{(\Delta\eta)^2 + (\Delta\phi)^2} \tag{3.6}$$

which is also invariant under axial boosts by construction.

3.2.3 Phenomenological variables

When protons collide at the center of the detector, only some of the partons (valence quarks, gluons and sea quarks) of each proton take part in the interaction. They can carry different fractions of the total proton momentum, which means the opposite momenta do not cancel each other out. Instead, the particles involved have a randomly distributed total momentum along the beam axis, which means that all collision products get a Lorentz boost parallel to the z-axis. Consequently, it is practical to use quantities invariant under such boosts.

For ultrarelativistic particles, one such quantity is $\Delta\eta$ as introduced in the previous section. Another one, which is applicable to all particles, is the *transverse momentum*

$$p_\mathrm{T} = \sqrt{p_x^2 + p_y^2} \tag{3.7}$$

$$= \sqrt{p^2 - p_z^2} \tag{3.8}$$

$$= \frac{p}{\cosh\eta} \tag{3.9}$$

Therefore, this quantity is often used instead of the full particle momentum. Related to transverse momentum is *transverse energy*

$$E_\mathrm{T} = \sqrt{m^2 + p_\mathrm{T}^2} \tag{3.10}$$

$$= \sqrt{E^2 - p_z^2}. \tag{3.11}$$

Neutrinos only interact via the weak force, which means the vast majority of them does not interact with the material of the particle detector. However, the sum of their transverse momenta can be inferred if all other particle momenta are known, since the transverse momentum of the initial state is known to be zero. This is called the *missing transverse energy*

$$E_\mathrm{T}^\mathrm{miss} = \sqrt{\left(\sum_i p_{i,x}\right)^2 + \left(\sum_i p_{i,y}\right)^2}. \tag{3.12}$$

Collisions commonly produce an intermediate particle, which then decays to multiple products. The mass M of the intermediate particle can be reconstructed with the formula

$$M = \sqrt{\left(\sum_i E_i\right)^2 - \left|\sum_i \vec{p}_i\right|^2} \tag{3.13}$$

where the index i runs over all decay products. The quantity defined by this formula is often referred to as the *invariant mass*, and is also used regardless of whether the final-state particles are all the decay products of a single particle.

3.3 The ATLAS detector

ATLAS is an acronym for "A Toroidal LHC ApparatuS". The detector assembly has a total height and width of 25 m, a length of 44 m and a mass of about 7000 tons. It consists of multiple layers, each used to detect different particles. A brief overview of the individual components of the detector is given in the following sections.
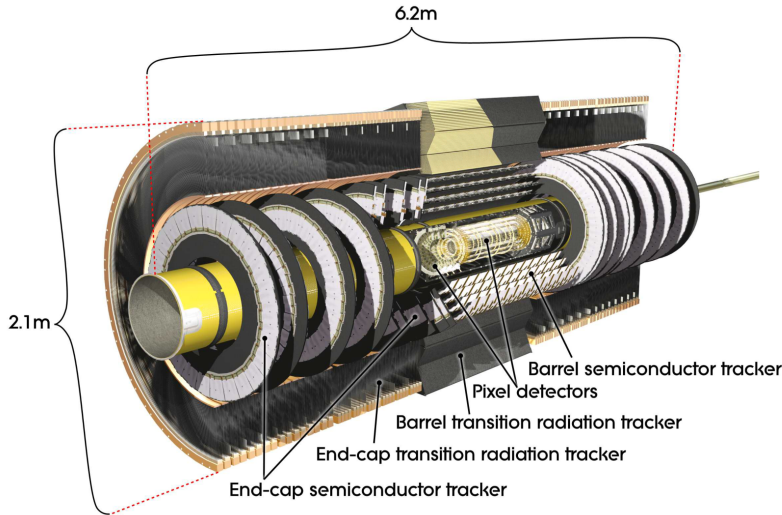
3.3.1 Inner Detector

Figure 3.3: Cut-away view at the ATLAS Inner Detector. [41]

The Inner Detector is used to record the tracks of charged particles. It is permeated by a magnetic field with a strength of 2 T, which is produced by a superconducting solenoid magnet aligned along the beam axis. This magnetic field deflects charged particles and causes their tracks to become curved, with the curvature radius dependent on the particle's charge and transverse momentum. This makes it possible to reconstruct not only the particle type and initial flight direction, but also the momentum.

To accurately measure the particle tracks, the Inner Detector is made up of three independent tracking systems: The Pixel Detector, Semiconductor Tracker (SCT) and Transition Radiation Tracker (TRT). They are arranged in concentric cylinders around the beam axis in the *barrel region*, with additional disk-shaped *endcaps* to also measure particles withh high pseudorapidity.

Closest to the interaction point at the center is the Pixel Detector, which achieves the highest resolution. It consists of over 80 million silicon pixels with a typical size of $50\,\mu m^2 \times 400\,\mu m^2$. The pixels are placed in four layers to provide an accuracy of $10\,\mu m$ in the $R - \phi$ plane and $115\,\mu m$ along the z-axis. The innermost layer is the Insertable B-Layer (IBL) [49], which was added for Run 2 to decrease the distance between Pixel Detector and interaction point.

The next detector layer is the Semiconductor Tracker, which uses silicon like the Pixel Detector, but arranged in thin strips both parallel and perpendicular to the beam axis. The 6.3 million readout channels allow an accuracy of $17 \, \mu m \times 580 \, \mu m$ $((R - \phi) \times z)$.

The outermost tracking layer, the Transition Radiation Tracker, uses a different detection method: It contains polypropylene foils and fibers with different refraction indices. When charged particles enter and exit the plastic, they emit transition radiation due to the change in refraction index, depending on the particle velocity. The TRT uses around 300 000 tubes filled with a gas mixture, each with a diameter of $4 \, mm$, to detect the transition radiation. When the gas is ionized by the radiation, it produces an electrical signal between a wire anode and the tube wall. [41]
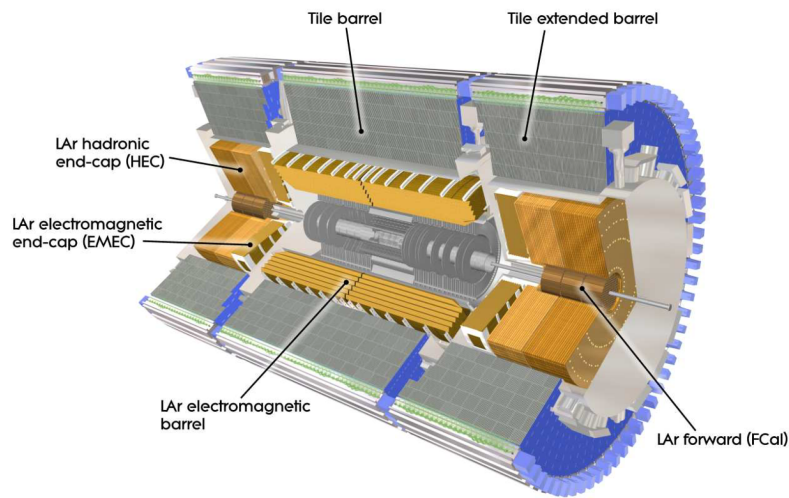
3.3.2 Calorimeter system

Figure 3.4: Cut-away view at the ATLAS calorimeter system. [41]

The ATLAS calorimeter system is built around the Inner Detector and measures the energies of the collision products. It is divided into the electromagnetic calorimeter, which mostly stops electrons and photons, and the hadronic calorimeter, which is built to measure the energy input from hadrons like protons, neutrons and pions.

The electromagnetic (EM) calorimeter consists of lead absorber plates as well as liquid argon (LAr) detector material between the absorbers and copper readout electrodes. Incoming highly energetic electrons enter the absorber plates and emit bremsstrahlung. The radiated photons in turn produce electron-positron pairs, which leads to an electromagnetic shower. The lower-energetic electrons produced in the shower ionize the liquid argon, which results in a measurable current due to the electric field between the absorber plates and the readout electrodes. The resulting signal is proportional to the total energy of the electromagnetic shower.

The hadronic calorimeter works similarly to the EM calorimeter, but it is optimized

for hadronic showers from the strong interaction between energetic hadrons and the absorber nuclei. In the barrel region, the ATLAS detector uses a tile calorimeter with steel absorbers and scintillator tiles as the active material to produce an electrical signal. In the end caps and forward region, copper plates and liquid argon as in the EM calorimeter are used instead. [41]

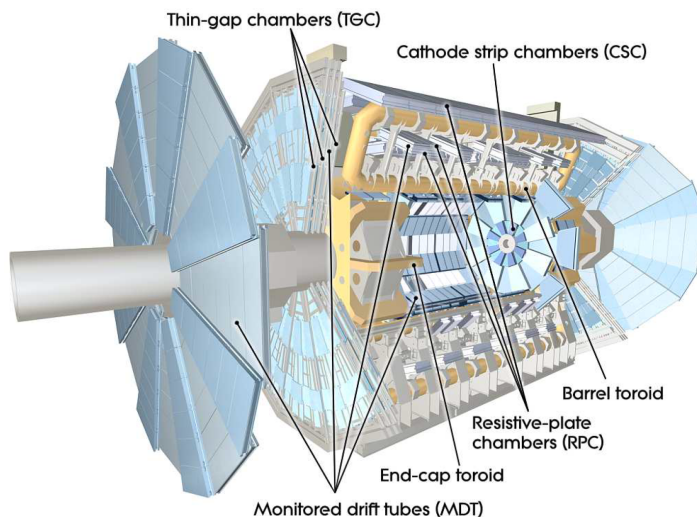### 3.3.3 Muon spectrometer

Figure 3.5: Cut-away view at the ATLAS muon system. [41]

Muons are about 200 times as massive as electrons, and consequently they experience a much lower acceleration due to the nuclear electric fields inside the detector material. Therefore, they produce bremsstrahlung at a much lower rate and travel through the detector almost unhindered, only losing a small amount of energy to ionization along the path. The muon spectrometer detects these muons and records their tracks. To also be able to measure the momentum of the muons, three toroidal superconducting magnets curve the muon trajectories.

The muon spectrometer consists of gas-filled chambers with an electric field applied to the gases. When a muon passes through the spectrometer, it ionizes the gas, creating free electrons and ions. There are various types of muon chambers used in the ATLAS detector, which use different methods to detect and/or locate the ionization: Monitored Drift Tubes provide general tracking, Cathode Strip Chambers are used for tracking specifically in the end caps, and Resistive Plate Chambers in the barrel together with Thin Gap Chambers in the end caps provide accurate fast reactions for triggers and coincidence measurements. [41]

4 Monte Carlo generators

To test theories of high-energy physics using modern particle colliders, it is indispensable to be able to make accurate theoretical predictions about interactions which produce a large number of reaction products. While for cross-sections of relatively simple QFT processes it is possible to calculate results through deterministic methods, this quickly becomes infeasible for higher numbers of involved particles. Additionally, traditional perturbative calculations of QCD processes diverge in the infrared regime. Monte Carlo methods solve the problem of high dimensionality by using a probabilistic approach, approximating integrals by randomly sampling from a distribution with given density. This approach makes it possible to perform QFT calculations which include the showers of color-charged particles typical for hadron colliders.

Monte Carlo event generators can simulate full events from the two colliding protons up to the final state entering the detector, as illustrated in figure 4.1. It is useful to split the simulation into several event phases. Each of them has distinct characteristics, so different approximations are necessary in every phase [50]:

- In a collision between protons, the initial interaction is **parton scattering** between the constituent quarks, sea quarks and gluons which make up the two protons. This phase is modeled using parton density functions (PDFs), which describe the energy-scale-dependent probability that a parton with a given momentum takes part in the interaction. PDF sets are fitted to the experimental data by various collaborations and can be used through the LHAPDF library [51].

- The **hard process** is the most important part of the event, and might include e.g. the production and decay of a Higgs boson. This phase is included in the simulation by evaluating the *matrix element* of the process. Due to the high energy scale, it can be calculated in fixed order perturbation theory.

- In the **parton shower** phase, particles with color charge interact through the strong force, which results in a cascade of particles with lower energies. Due to the decreasing energy scale, the shower can be approximated well by factorizing it into smaller processes.

- Below an energy scale of a few hundred MeV, **hadronization** takes place due to the nonperturbative confinement of quarks. This is simulated with a phenomenological fragmentation model.

- Most resonances created during hadronization quickly undergo **hadron decays** into longer-lived particles. Event generators simulate the decay branching ratios and kinematics using experimentally measured values and fitted models.

- If the state resulting from the previous phases includes relatively long-lived but nonetheless unstable particles, their **later decays** have to be simulated separately.

- The **underlying event** summarizes all reactions of the colliding protons which are not included in the hard event. Additionally, the **pile-up** describes products of other proton collisions which are also detected within the same event, whether from the same bunch crossing (*in-time* pile-up) or another crossing within the detector readout time (*out-of-time* pile-up). These secondary processes are mostly simulated the same way as the results of the hard event, and their rate and distribution is fitted to the measured pile-up profile in each data-taking period.
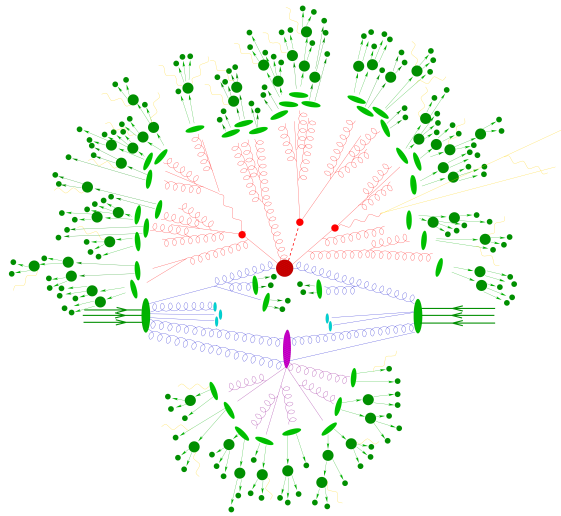

Figure 4.1: Illustration of the processes involved in a proton-proton collision process, as simulated by a Monte Carlo event generator. It includes scattering of the partons (blue), hard process (dark red circle), parton shower (red), underlying event (purple), hadronization (light green), decay (dark green) and radiation (yellow). [50]

For each event produced by the Monte Carlo generator, the final state is used as input for a simulation of detector hits. From there, the reconstruction and analysis process can be applied to generated samples in the same way as for real data events.

Due to the many numerical approximations, imperfect phenomenological models and uncertain theoretical parameters, the simulated results sometimes deviate from the data, even without the presence of new physical phenomena. Therefore, various ad-hoc techniques are employed to correct the generated distributions, such as scale factors and parameter-dependent reweighting. The potential discrepancy between simulation and reality also means that it is important to investigate the systematic uncertainties in Monte Carlo predictions and to take them into account when calculating significances and limits.

In this analysis, the decay processes of weak bosons ($Z \to ll$, $W \to l\nu$, Diboson) are simulated using `SHERPA v2.2` [52], while SM Higgs and top quark processes use `PYTHIA v8.2` [53] together with `POWHEG-BOX v2` [54] for the matrix element and matching procedure. Additionally `MadGraph5_aMC@NLO` [55] and `HERWIG 7` [56] are used for alternative samples to estimate systematic uncertainties.

5 Analysis

The analysis is based on the flavor-aligned 2-Higgs doublet model (2HDM), which could explain the deviation in the anomalous magnetic moment of the muon (see section 2.2). This model introduces 4 additional Higgs bosons, among them the CP-odd A boson.

To be able to explain the experimental value of a_μ, the A boson needs to have a mass below about $100\,\mathrm{GeV}$, and should couple strongly to leptons and up-type quarks. If this is the case, it should be possible to detect the production and decay of A bosons at the ATLAS detector.
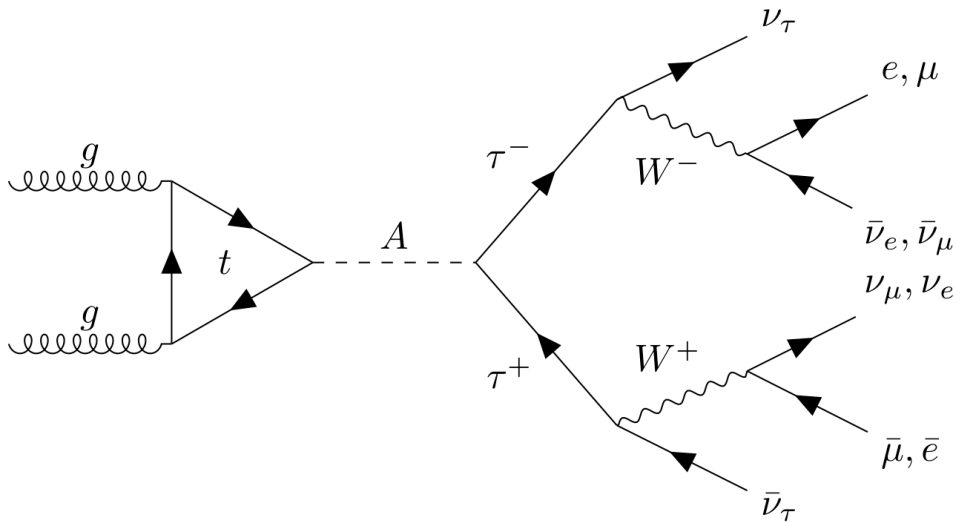
5.1 Signal process

Figure 5.1: Feynman diagram of the signal process used in the analysis, including production and decay of the A boson. [21]

The A boson interacts with all fermions due to the Yukawa coupling terms. The coupling strength is proportional to the fermion mass and the applicable coupling parameter ζ_u, ζ_d or ζ_l. With the parameter values necessary to explain Δa_μ, top quarks and tau leptons have by far the strongest coupling to A bosons. Consequently, A bosons are produced mainly via gluon fusion with a top quark loop, and they decay to $\tau^+\tau^-$ with a very high probability. At the hypothesized A boson masses, a decay to $t\bar{t}$ is kinematically implausible.

Decay mode	Branching ratio
Leptonic	
$e^-\bar{\nu}_e\nu_\tau$	17.82 %
$\mu^-\bar{\nu}_\mu\nu_\tau$	17.39 %
Hadronic	
$h^-\nu_\tau$ (1-prong, no neutrals)	11.51 %
$h^-n^0\nu_\tau$ (1-prong with neutrals)	37.01 %
$h^-h^-h^+\nu_\tau$ (3-prong)	14.55 %
others	1.72 %

Table 5.1: Decay channels of the tau lepton and their branching ratios. [57]

The two tau leptons have various hadronic and leptonic decay modes (see table 5.1). Due to the low A boson mass, the hadronic decay modes are overshadowed by hadronic jets from QCD events, which are very abundant at low energies. The ATLAS trigger system rejects most events with such low-energetic hadronic jets, since they are too frequent to record all of them.

For the remaining leptonic decay modes, the most significant background of lepton pairs comes from $Z \rightarrow ee$ and $Z \rightarrow \mu\mu$ processes. These can be excluded by requiring one electron and one muon in the final state, as shown in figure 5.1. The total branching ratio for this $A \rightarrow \tau\tau \rightarrow e\,\mu\,4\nu$ decay is 6.2 %.

5.2 Background processes

5.2.1 $Z \rightarrow \tau\tau$

The decay of the Z boson to two tau leptons (see fig. 5.2) is the most important background process for this analysis, since it produces the same $\tau^+\tau^-$ state as the signal process.

Separating A- and Z bosons by their reconstructed masses is difficult, since the neutrinos in the final state carry momentum which cannot be measured by the detector. An estimation of the mass of the decaying boson is still possible, but the achievable resolution is limited. At 91 GeV, the Z boson mass also falls into the range of A boson masses considered in this analysis, so a discrimination based on mass is essentially impossible for hypotheses with M_A close to 90 GeV.

Other differences between the A and Z bosons are their spin and parity. The A boson is pseudoscalar (spin 0, $P = -1$) and CP-odd, while the Z boson has spin 1 and is not an eigenstate of the parity operator.

This influences the angle between the tau lepton decay products. For the decay of a CP-odd particle like the A boson, the two tau leptons need to have antiparallel spins, while for a CP-even parent particle like a SM Higgs boson, the spins would need to be parallel to conserve the CP eigenvalue. Each tau lepton decays via a W boson, which only couples to the left-handed component of the τ^- and the right-handed component of the
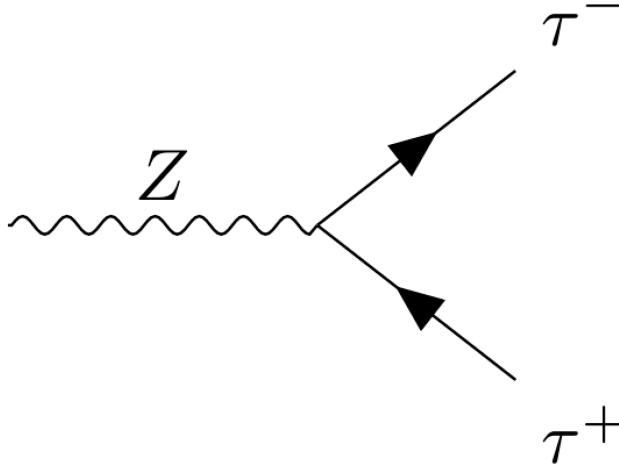
Figure 5.2: Feynman diagram of the background process $Z \to \tau\tau$. [21]

τ^+. Therefore the direction of the tau spin affects the direction of its decay products. In the CP-odd case with antiparallel spins, the tau lepton decay planes are close to parallel in most cases, which leads to a lower angular separation ΔR between the visible decay products. With a CP-even Higgs, the opposite effect results in a higher ΔR, while the angular distribution for Z boson decays lies in between (see fig. 5.3).

5.2.2 $Z \to ee$, $Z \to \mu\mu$

Instead of decaying via the $\tau\tau$ intermediate state, the Z boson can also directly decay into a pair of electrons or a pair of muons, with no additional neutrinos, as shown in figure 5.4.

Requiring one electron and one muon in the final state supresses such Z decays. The resulting background rejection is very valuable, since other discriminating variables such as missing transverse energy would not be accurate enough, and justifies the halved signal strength.

The remaining contribution of electronic and muonic Z boson decays is due to the possibility of particle misidentification during the reconstruction process.

5.2.3 Top quark decays

Top quarks decay nearly exclusively via the weak interaction into a bottom quark and a W^+ (see fig. 5.5). The resulting W boson can produce quark-antiquark or lepton-neutrino pairs, with a branching ratio of 11 % each for electrons, muons and tauons. [57]

As a result, the decay of $t\bar{t}$ pairs can produce an electron and a muon like the signal process. The main difference is the presence of bottom quarks in the final state, which can be used to suppress the $t\bar{t}$ background. The bottom quarks form B-mesons, and
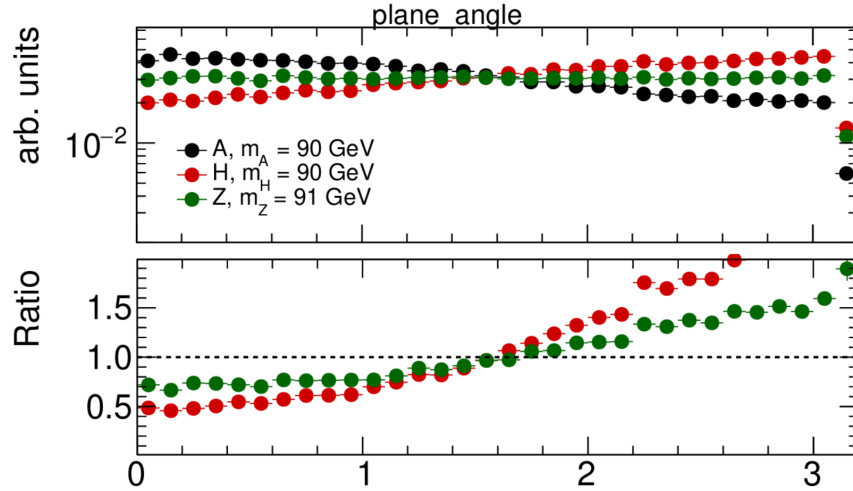
Figure 5.3: Distribution of the angle between the tau lepton decay planes, for a CP-odd Higgs boson A (black), a CP-even Higgs boson H (red) and a neutral weak gauge boson Z (green) as the parent particle. [21]

the resulting hadronic jets can be identified by a b-tagging algorithm [58]. Rejecting all events which include such a b-tagged jet reduces the background from all top quark decay processes. Unfortunately, the b-tagging algorithm only has an efficiency of 85 %, so $t\bar{t}$ still contributes significantly to the background.

The decay of a single top quark only produces a maximum of one electron or muon, so it cannot result in an $e\mu$ final state on its own. Only when combined with leptons from a different source, such as the underlying event, pile-up or a misidentified jet, can it contribute to the background.

5.2.4 Diboson processes

W bosons can decay into an electron or a muon (with associated neutrinos) either directly or through an intermediate tau lepton, as shown in figure 5.6. A pair of such leptonically decaying W bosons can result in the same final state as the signal process, with one electron and one muon together with missing energy in the form of neutrinos. The best procedure to distinguish between the two processes is through mass variables, which typically have a higher value for WW decays than for the signal process.

The Diboson category additionally includes all other processes involving two weak bosons (WW, WZ and ZZ). These can result in a wide range of final states, some of them similar to the target signature. Final states other than $e\mu$ can also contribute if a particle is misidentified or escapes undetected.
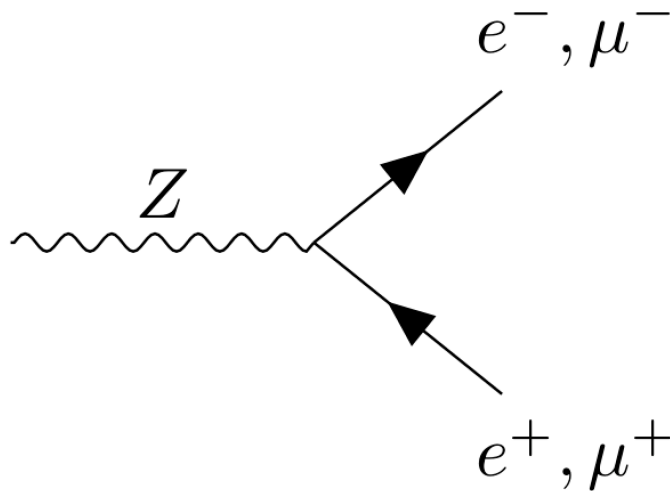
Figure 5.4: Feynman diagram of the background process $Z \to ee/\mu\mu$. [21]

5.2.5 $W \to l\nu$

Single W bosons frequently occur in proton-proton collisions as a result of quark-anti-quark annihilation. Similarly to single top quarks, their decay can only produce one lepton. Consequently, this process needs to coincide with a stray or fake lepton, which limits the size of this background.

5.2.6 SM Higgs decay

Like the A and Z bosons, the Standard Model Higgs boson can also decay into two tau leptons and thus result in the same final state as the signal process. Fortunately, the SM Higgs only has a low branching ratio of 6.2 % for $H \to \tau\tau$ [57], which results in a lower cross-section than for the signal process. Another channel for the SM Higgs to decay into $e\mu$ is via $H \to WW \to e\,\mu\,2\nu$, which also has a low total branching ratio.

The SM Higgs has a mass of 125 GeV, which is far enough outside the A boson mass range to allow for a good separation by mass variables. Additionally, the SM Higgs is even under the CP operation, therefore its decays are further supressed by the same angular cut used to reduce the $Z \to \tau\tau$ background.

5.2.7 QCD processes

The protons colliding inside the ATLAS experiment interact first and foremost via the strong interaction, so every event involves a large number of QCD processes. These naturally produce hadronic final states, which form cone-shaped jets inside the detector. It is possible for these hadronic jets to be falsely reconstructed as "fake" leptons. To result in the same signature as a signal event, either one fake lepton has to coincide with one real lepton from a background process, or two jets have to be misidentified in the
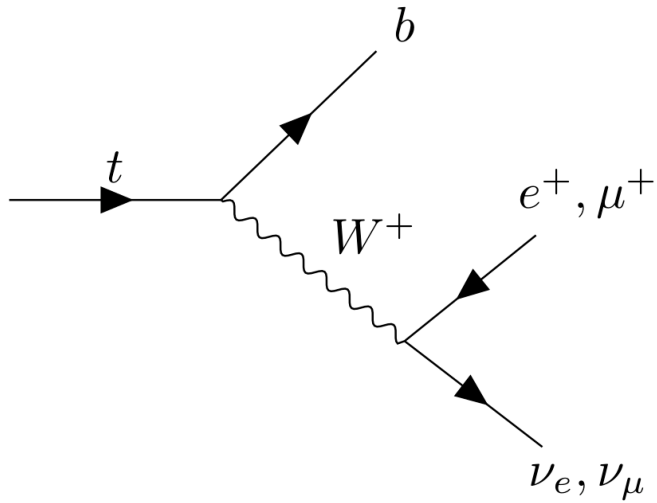
Figure 5.5: Feynman diagram of the leptonic decay of a top quark. [21]

same event. The former background is labeled by the respective process producing the real lepton, while the latter is called the "Multijet" or "Double-fake" background.

The abundance of misidentified jets is kept small by choosing strict identification criteria, which trade some signal strength for a lower probability of fake leptons. Additionally, hadronic jets typically have a detector signature spread out over a certain area. To take advantage of this, an *isolation criterion* is used, which rejects lepton tracks with jet signatures nearby and thereby increases the specifity of the reconstruction.
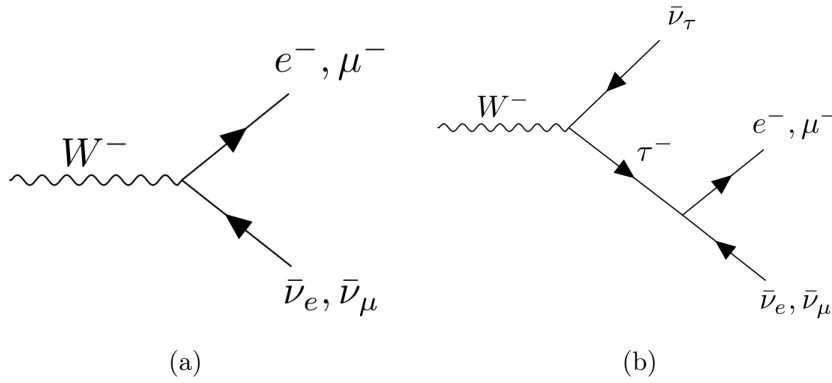
Figure 5.6: Feynman diagram of the W boson decays $W \to l\bar{\nu}_l$ (a) and $W \to \tau\nu_\tau \to l\bar{\nu}_l\nu_\tau$ (b). [21]

5.3 Signal region event selection

5.3.1 Triggers

Collisions at the ATLAS detector have to activate one of the triggers implemented in the Trigger and Data Aquisition system in order to be processed and recorded onto storage. This analysis uses events from three different electron-muon triggers, namely `e7mu24`, `e17mu14` and `e26mu8`, which record events in which the leading and subleading leptons are an electron and a muon (or vice versa) with transverse momenta above the respective trigger thresholds. The p_T-regions for each trigger are further restricted by analysis-level cuts to ensure that accurate trigger efficiency simulations are available and that the regions for different triggers do not overlap. The resulting ranges are shown in figure 5.7.

5.3.2 Mass variables

Since the final state of the signal process includes neutrinos, the mass of the A boson cannot be fully reconstructed from the invariant mass of its visible decay products. For the neutrinos, only the sum of their transverse momenta can be inferred from the missing transverse energy $E_{\mathrm{T}}^{\mathrm{miss}}$. Instead, two variables are used which approximate the mass of the parent particle.

The total transverse mass is defined as the invariant mass calculated from the electron and muon transverse momenta together with the missing transverse energy:

$$m_{\mathrm{T}}^{\mathrm{tot}} = \sqrt{\left(p_{\mathrm{T}}^e + p_{\mathrm{T}}^\mu + E_{\mathrm{T}}^{\mathrm{miss}}\right)^2 - \left|\vec{\mathbf{p}}_{\mathrm{T}}^e + \vec{\mathbf{p}}_{\mathrm{T}}^\mu + \vec{\mathbf{E}}_{\mathrm{T}}^{\mathrm{miss}}\right|^2} \tag{5.1}$$

Including $E_{\mathrm{T}}^{\mathrm{miss}}$ makes this variable a more precise estimate of the full invariant mass than a definition based only on the visible leptons. In this analysis, $m_{\mathrm{T}}^{\mathrm{tot}}$ is mainly used as a cut parameter.

The Missing Mass Calculator (MMC) uses a likelihood-based approach to reconstruct-
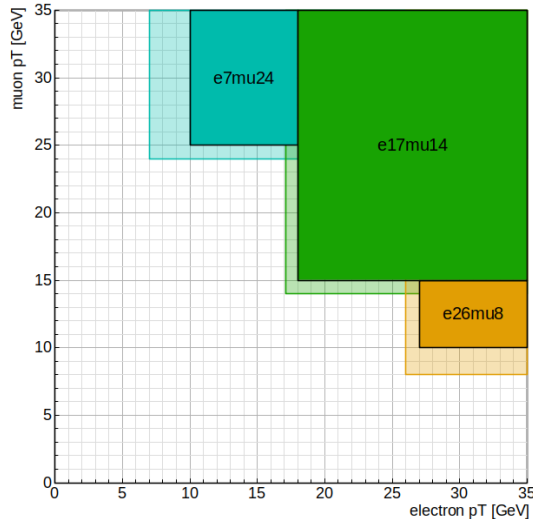
Figure 5.7: Ranges of electron and muon transverse momentum for the different triggers. The trigger regions are separated by p_T cuts, i.e. there is no region with multiple triggers in use. The transparent regions fire the trigger but are excluded for the analysis.

ing the parent particle mass. It tries to reconstruct the full decay kinematics, including the momentum and invariant mass of the neutrino pair resulting from each tau decay. The MMC takes into account the measured momenta of the leptons and the missing transverse energy, together with their relative orientations, to reduce the problem down to a four-dimensional space of unknown parameters. Within that parameter space, it uses the known probability density function for the angular separation ΔR between visible and invisible tau lepton decay products to define a likelihood function. The value of the invariant mass at the point with the highest likelihood is used as the estimate m_{MMC}. This MMC mass estimate is used as the main mass variable in this analysis.

5.3.3 Cuts

Events are required to have exactly one electron and one muon; the presence of additional leptons causes a veto. Since the A boson is neutral, the electron and muon need to have opposite charges.

Since the signal process yields neutrinos with substantial energies (due to the kinetic energy released from tau decay), it is more likely to have a high missing transverse energy than most backround processes. Therefore, a cut is used to remove events with a low $E_{\mathrm{T}}^{\mathrm{miss}}$.

Another useful property to increase the signal-to-background ratio is the low mass of the A boson. Background processes such as Top and Diboson have intermediate states with higher masses, so it makes sense to exclude these with a cut imposing a maximum on the total transversal mass.

Region		Signal Region		Same-sign VR		Top VR	$Z \to \tau\tau$ VR
		low-mass	high-mass	low-mass	high-mass		
Missing E_T cut	E_T^{miss}	$> 50\,\mathrm{GeV}$	$> 30\,\mathrm{GeV}$	$> 50\,\mathrm{GeV}$	$> 30\,\mathrm{GeV}$	$> 30\,\mathrm{GeV}$	$-$
Mass cut	m_T^{tot}	$< 45\,\mathrm{GeV}$	$< 65\,\mathrm{GeV}$	$< 45\,\mathrm{GeV}$	$< 65\,\mathrm{GeV}$	$< 65\,\mathrm{GeV}$	$< 65\,\mathrm{GeV}$
Angular cut	ΔR_{ll}	< 0.7	< 1.0	< 0.7	< 1.0	< 1.0	> 1.4
MMC cut	m_{MMC}	$> 0\,\mathrm{GeV}$	$> 35\,\mathrm{GeV}\,\&$ $< 130\,\mathrm{GeV}$	$> 0\,\mathrm{GeV}$	$> 35\,\mathrm{GeV}\,\&$ $< 130\,\mathrm{GeV}$	$> 0\,\mathrm{GeV}$	$> 0\,\mathrm{GeV}$
Charge cut	$q_e \cdot q_\mu$	-1	-1	**1**	**1**	-1	-1
b-tag	$n_{b\text{-jets}}$	0	0	0	0	$> \mathbf{0}$	0

Table 5.2: Overview of the cuts for the different regions.

Finally, an angular cut is used to discriminate against the $Z \to \tau\tau$ background, as discussed in section 5.2.1. This cut only accepts events with an angular separation between the two leptons

$$\Delta R_{ll} = \sqrt{(\eta_e - \eta_\mu)^2 + (\phi_e - \phi_\mu)^2} \tag{5.2}$$

below a threshold value.

The cutoff values for all cut variables are optimized separately for low mass hypotheses from 20 to 80 GeV (Low-Mass Signal Region, LMSR) and high mass hypotheses from 80 to 110 GeV (High-Mass Signal Region, HMSR). They are summarized in table 5.2.

The expected variable distributions for the background in the low-mass and high-mass variants of the Signal Region are plotted in figures 5.8 and 5.9.
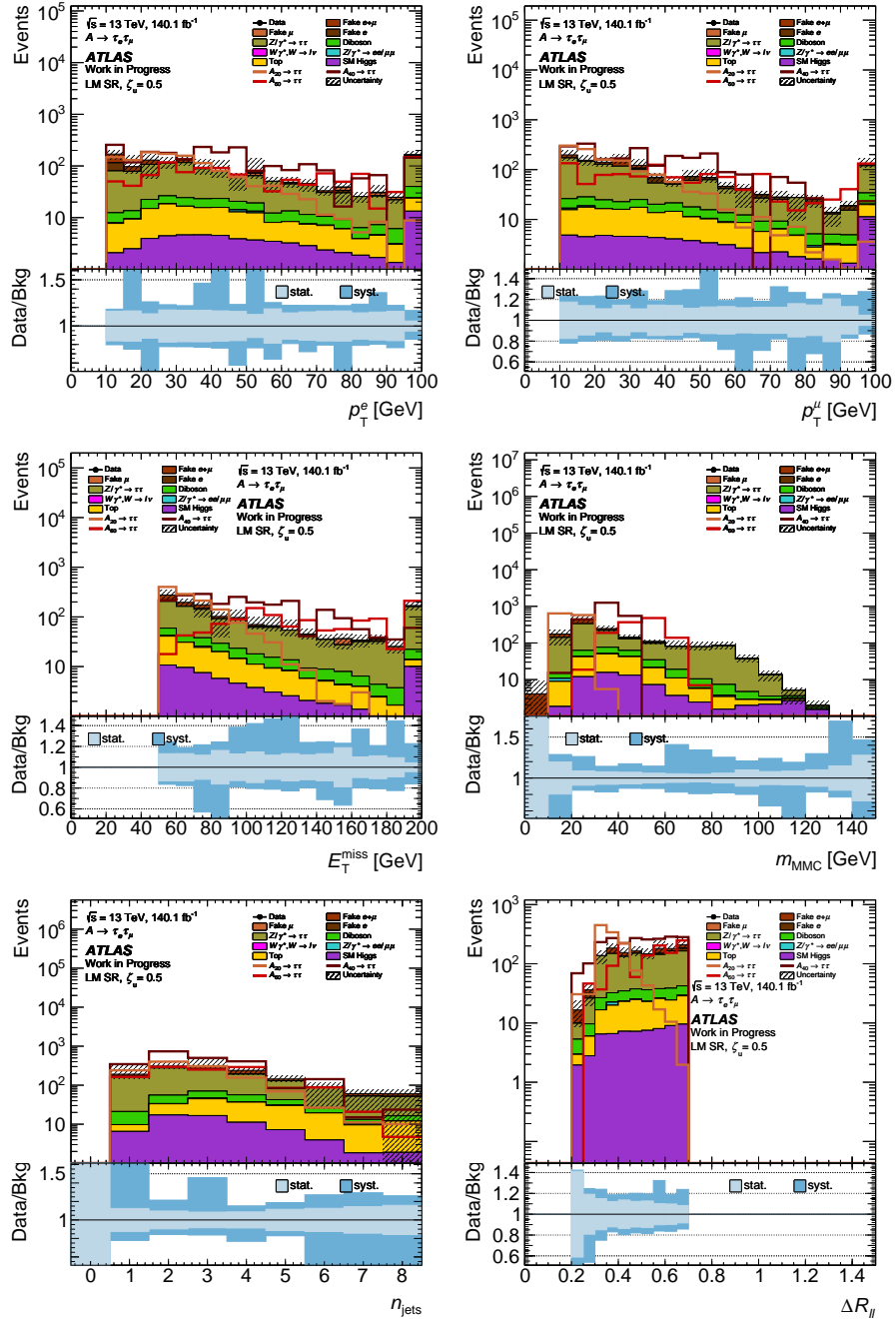
Figure 5.8: Variable distributions for the expected background in the low-mass Signal
Region after applying all cuts. Event counts are plotted logarithmically. The
fake lepton backgrounds are estimated using the matrix method, all others
are modeled using Monte Carlo samples. The shaded bands in the ratio
plots show the statistical and systematic uncertainties. The last bin includes
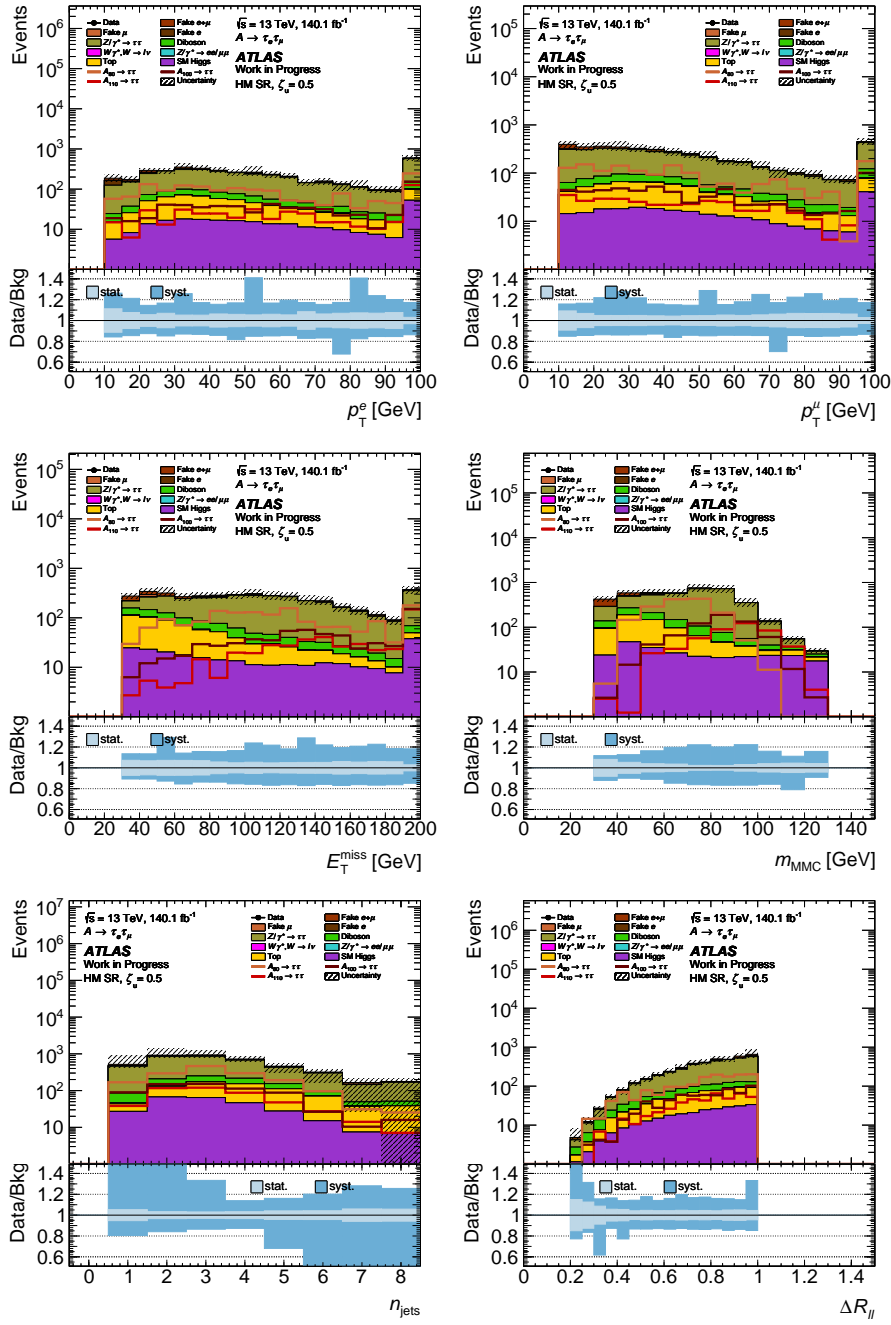overflow, i.e. events with values above the plotting range.

34

Figure 5.9: Variable distributions for the expected background in the high-mass Signal Region after applying all cuts. Event counts are plotted logarithmically. The fake lepton backgrounds are estimated using the matrix method, all others are modeled using Monte Carlo samples. The shaded bands in the ratio plots show the statistical and systematic uncertainties. The last bin includes overflow, i.e. events with values above the plotting range.

5.4 Background estimation and validation

The contribution of misidentified QCD jets is modeled separately, using a data-driven estimation method (see section 5.5). For all other backgrounds, Monte Carlo simulations are used.

Since all these estimation methods are not guaranteed to accurately fit reality, it is important to check the agreement between the model and the data. This is done by comparing the real and predicted background event distributions in validation regions (VRs). To keep the analysis blinded while adjusting the background estimation, these VRs need to be orthogonal to the Signal Region (i.e. events in the SR cannot also be accepted by the VR cuts), and they should not be expected to include a significant number of events from the signal process. The cuts used in different regions are listed in table 5.2.

5.4.1 $Z \rightarrow \tau\tau$ Validation Region

The $Z \rightarrow \tau\tau$ Validation Region (ZVR) is mainly used to check the modeling of the $Z \rightarrow \tau\tau$ process, since it produces the most dominant background. To enhance the contribution of Z boson decays while suppressing the signal in the ZVR, the angular cut is inverted to $\Delta R_{ll} > 1.4$. The cut $m_{\mathrm{T}}^{\mathrm{tot}} < 65\,\mathrm{GeV}$ is taken from the high-mass SR, together with the charge and b-tag requirements, to keep it similar to the Signal Region. The different variable distributions of background and data in this region are shown in figure 5.10.

5.4.2 Top Validation Region

In the Top Validation Region (TVR), the b-tag cut is inverted: Instead of a veto on b-tagged jets, events are required to have at least one b-jet with $p_{\mathrm{T}} > 20\,\mathrm{GeV}$. This excludes most of the signal and boosts the proportion of top quark decays to allow a check of the top background modeling. The different variable distributions of background and data in this region are shown in figure 5.11.

5.4.3 Same-sign Validation Region

The Same-sign Validation Region (SSVR) uses an inverted cut on the lepton charges. The signal and the most important backgrounds involve a neutral resonance and therefore produce leptons with opposite charges. Requiring the leptons to have equal charge excludes these processes to get a higher percentage of events due to fake leptons. This is useful to test the modeling of jet misidentification and the data-driven estimation of the Multijet or total fake-related background. The different variable distributions of background and data in this region are shown in figure 5.12.
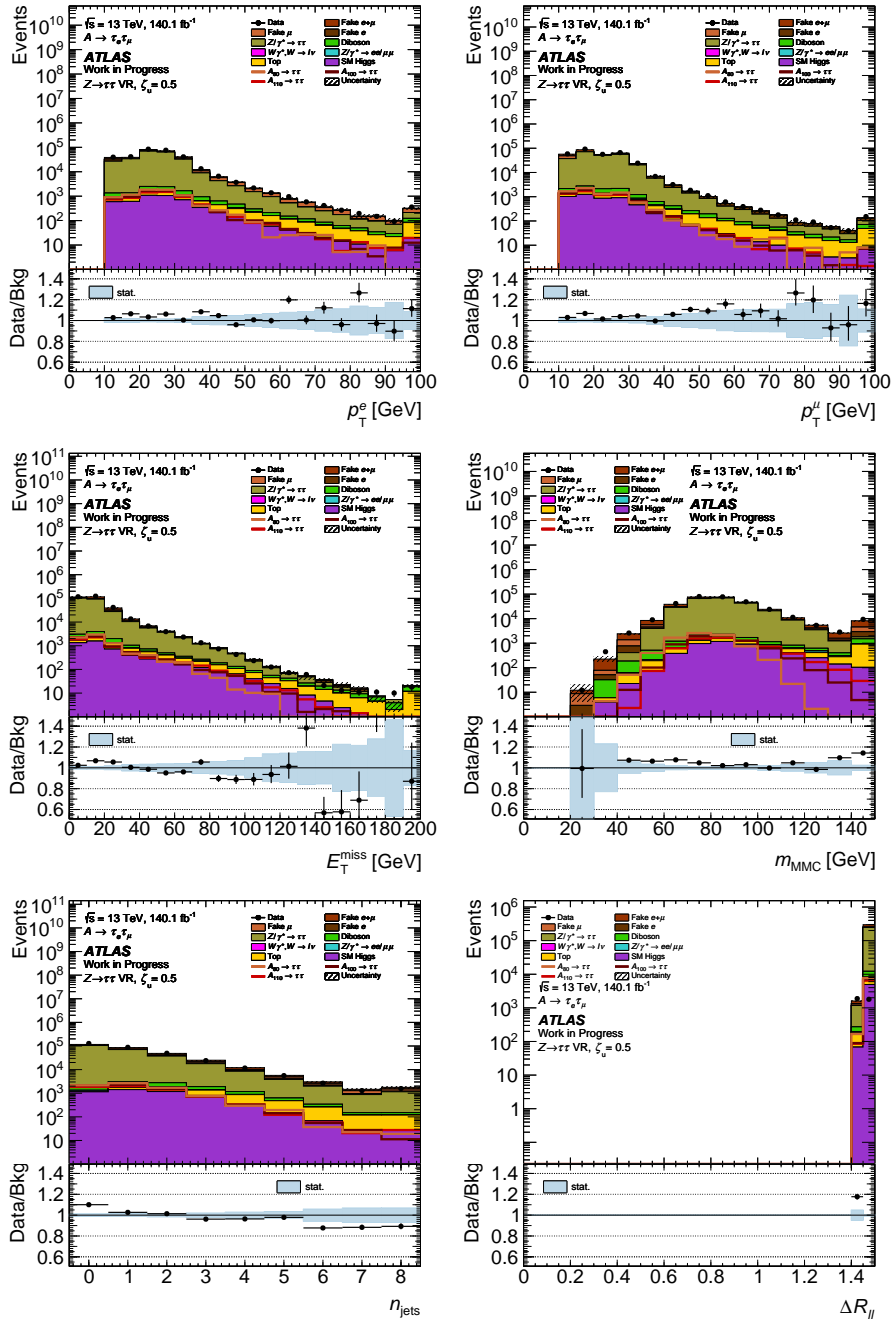
Figure 5.10: Variable distributions of data and background in the $Z \to \tau\tau$ VR. Event counts are plotted logarithmically. The fake lepton backgrounds are estimated using the matrix method, all others are modeled using Monte Carlo samples. The shaded bands in the ratio plots show the statistical uncertainties. The last bin includes overflow, i.e. events with values above the plotting range.
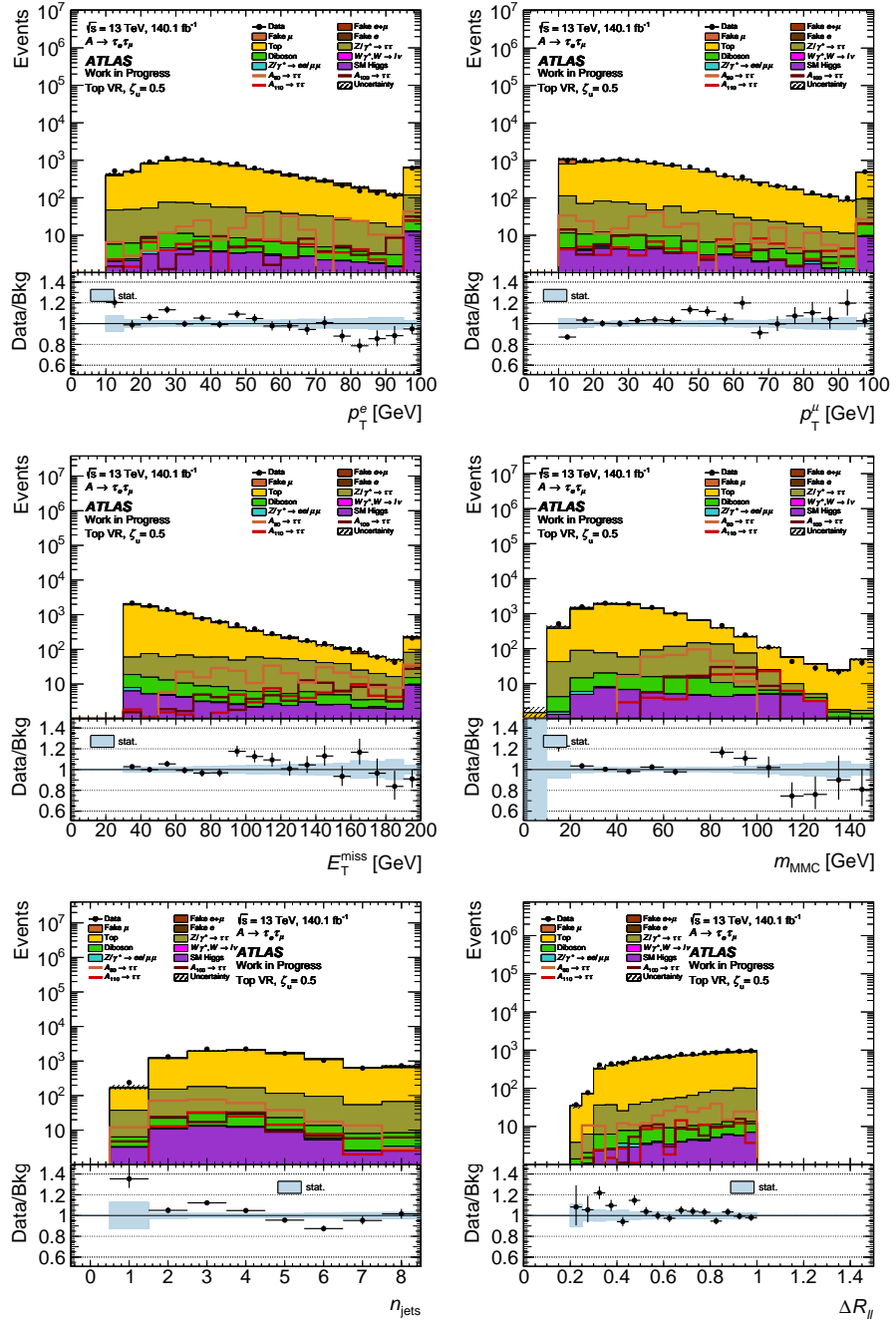
Figure 5.11: Variable distributions of data and background in the Top VR. Event counts are plotted logarithmically. The fake lepton backgrounds are estimated using the matrix method, all others are modeled using Monte Carlo samples. The shaded bands in the ratio plots show the statistical uncertainties. The last bin includes overflow, i.e. events with values above the plotting range.

Figure 5.12: Variable distributions of data and background in the (high-mass) Same-sign VR. Event counts are plotted logarithmically. The fake lepton backgrounds are estimated using the matrix method, all others are modeled using Monte Carlo samples. The shaded bands in the ratio plots show the statistical uncertainties. The last bin includes overflow, i.e. events with values above the plotting range.
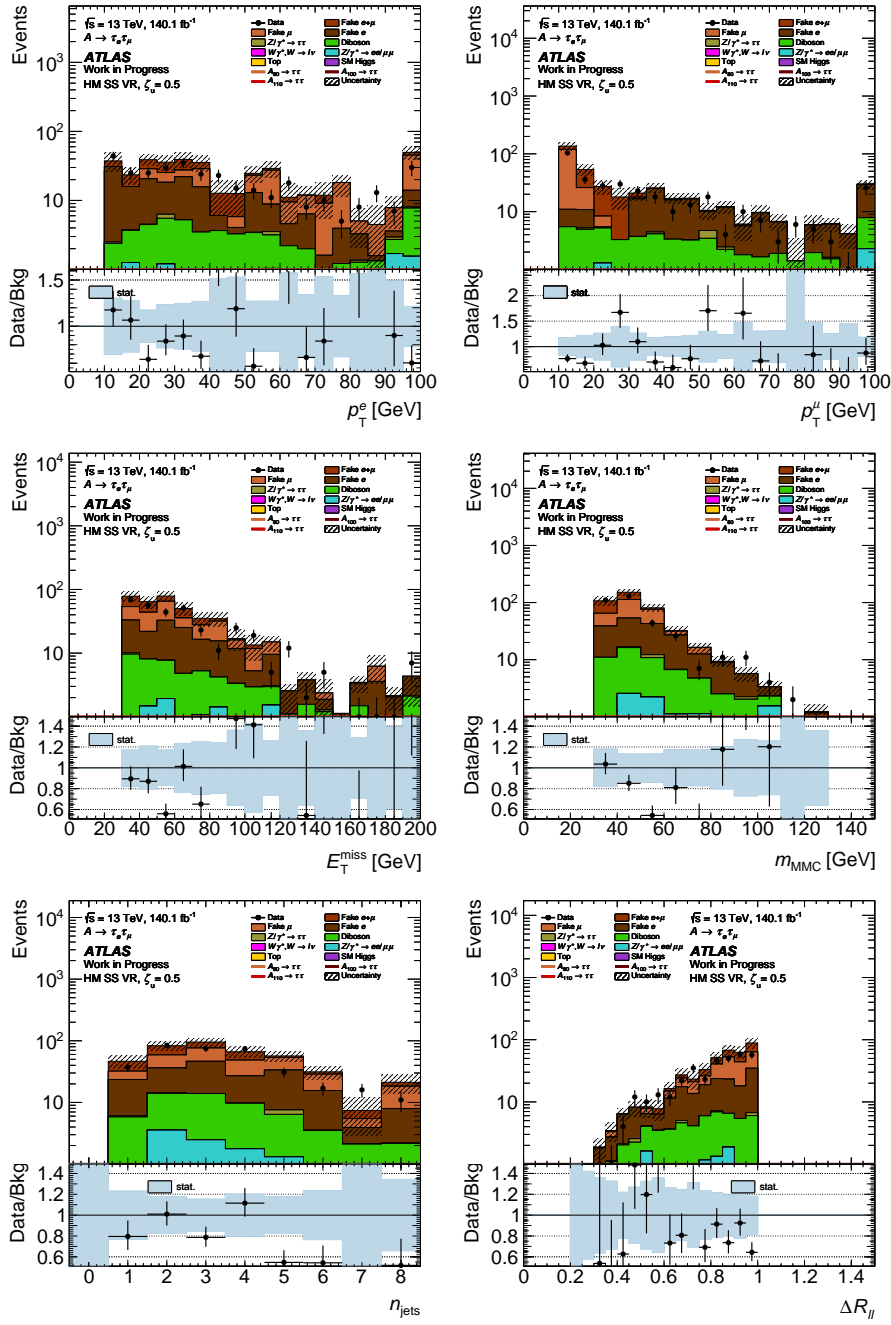
5.5 Jet fake background estimation

The distribution of hadronic jets is hard to simulate accurately with Monte Carlo methods due to the nonperturbative nature of QCD. For the Multijet background, the combination of high jet production cross-section and small acceptance presents another challenge for generating a statistically significant number of samples. Finally, the probability of a jet being misidentified as a lepton is not modeled well enough. As a result, it is not feasible to use Monte Carlo samples to model the Multijet background. Instead, two different data-driven methods are used to estimate the rate of fake leptons. The fake factor method was already used in previous versions of the analysis, while the matrix method was implemented at the request of the ATLAS Isolation and Fake Forum (IFF). The fake factor method is still used as a secondary estimate for validation.

5.5.1 Fake factor method

The fake factor method uses data from three additional regions in which at least one of the reconstructed leptons fails the tight isolation and/or identification criteria (see fig. 5.13). The quadrant with both leptons passing the criteria corresponds to the usual Signal or Validation Region. All cuts other than Iso/ID are kept the same across all four regions.
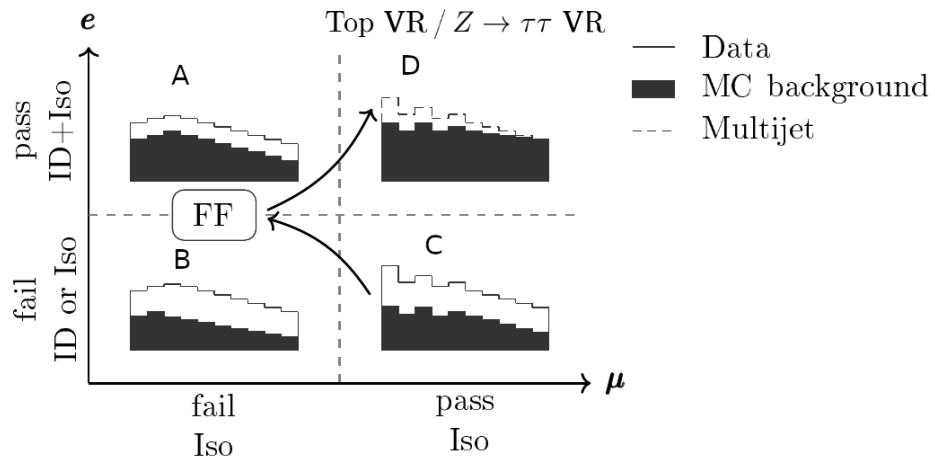

Figure 5.13: Schematic overview of the four regions used for fake lepton estimation, and the workflow of the fake factor method.

The method assumes that in an event with two fake leptons, the fake electron passing the Iso/ID criteria is statistically independent of the fake muon passing the isolation

40

criterion. The statistical independence condition can be formalized as

$$\frac{P(\text{pass electron} \wedge \text{pass muon})}{P(\text{fail electron} \wedge \text{pass muon})} = \frac{P(\text{pass electron} \wedge \text{fail muon})}{P(\text{fail electron} \wedge \text{fail muon})} \tag{5.3}$$

It is also assumed that in all non-signal regions, the difference between data and MC simulations is due to events with two misidentified jets. From this it is possible to calculate an estimate of the number of Multijet events with both leptons passing the criteria:

$$N_{e\,\text{pass},\,\mu\,\text{pass}}^{\text{Multijet}} = \frac{N_{e\,\text{pass},\,\mu\,\text{fail}}^{\text{Multijet}}}{N_{e\,\text{fail},\,\mu\,\text{fail}}^{\text{Multijet}}} N_{e\,\text{fail},\,\mu\,\text{pass}}^{\text{Multijet}} \tag{5.4}$$

$$= \text{FF} \cdot \left(N^{\text{Data}} - N^{\text{MC}}\right)_{e\,\text{fail},\,\mu\,\text{pass}} \tag{5.5}$$

$$\text{with} \quad \text{FF} = \frac{\left(N^{\text{Data}} - N^{\text{MC}}\right)_{e\,\text{pass},\,\mu\,\text{fail}}}{\left(N^{\text{Data}} - N^{\text{MC}}\right)_{e\,\text{fail},\,\mu\,\text{fail}}} \tag{5.6}$$

The *fake factors* FF are calculated as a function of the electron transverse momentum by binning the relevant data and MC numbers in p_{T}^{e}. [59]

5.5.2 Matrix method

In contrast to the fake factor method, the matrix method aims to model all background contributions involving any number of misidentified jets, without relying on e.g. $W \rightarrow l\bar{\nu}_l$ and single top MC samples. It also uses data from leptons which fail the tight isolation, but additionally needs independent measurements of the *efficiencies*. The real and fake efficiency ϵ_R^l and ϵ_F^l for a lepton type l are defined as the probability that a real/fake lepton from the baseline selection passes the tight isolation criteria.

Analogously to the fake factor method, four regions are defined based on the two leptons either passing or failing tight isolation criteria. They are abbreviated by e.g. TL for a tight electron (passing tight isolation) and a loose muon (not passing tight criteria). In each region, there are contributions from events with any combination of a real/fake electron and a real/fake muon. The expected number for each contribution is a product of the applicable efficency by the total events with the given combination of real/fake leptons. This gives a system of linear equations, which can be expressed in matrix form:

$$\begin{pmatrix} N_{\text{TT}} \\ N_{\text{TL}} \\ N_{\text{LT}} \\ N_{\text{LL}} \end{pmatrix} = \underbrace{\begin{pmatrix} \epsilon_R^e \epsilon_R^\mu & \epsilon_R^e \epsilon_F^\mu & \epsilon_F^e \epsilon_R^\mu & \epsilon_F^e \epsilon_F^\mu \\ \epsilon_R^e \bar{\epsilon}_R^\mu & \epsilon_R^e \bar{\epsilon}_F^\mu & \epsilon_F^e \bar{\epsilon}_R^\mu & \epsilon_F^e \bar{\epsilon}_F^\mu \\ \bar{\epsilon}_R^e \epsilon_R^\mu & \bar{\epsilon}_R^e \epsilon_F^\mu & \bar{\epsilon}_F^e \epsilon_R^\mu & \bar{\epsilon}_F^e \epsilon_F^\mu \\ \bar{\epsilon}_R^e \bar{\epsilon}_R^\mu & \bar{\epsilon}_R^e \bar{\epsilon}_F^\mu & \bar{\epsilon}_F^e \bar{\epsilon}_R^\mu & \bar{\epsilon}_F^e \bar{\epsilon}_F^\mu \end{pmatrix}}_{E_{e\mu}} \begin{pmatrix} N_{\text{RR}} \\ N_{\text{RF}} \\ N_{\text{FR}} \\ N_{\text{FF}} \end{pmatrix} \tag{5.7}$$

where $\bar{\epsilon} = 1 - \epsilon$. Solving the system of equations by inverting the matrix allows one to calculate the total numbers of events with fake leptons N_{RF}, N_{FR} and N_{FF} and therefore

also their contributions to the signal TT region:

$$N_{\mathrm{TT}}^{\mathrm{fake}} = \epsilon_{\mathrm{R}}^e \epsilon_{\mathrm{F}}^\mu N_{\mathrm{RF}} + \epsilon_{\mathrm{F}}^e \epsilon_{\mathrm{R}}^\mu N_{\mathrm{FR}} + \epsilon_{\mathrm{F}}^e \epsilon_{\mathrm{F}}^\mu N_{\mathrm{FF}} \tag{5.8}$$

The matrix inversion can easily be done analytically by writing the 4×4 efficiency matrix $E_{e\mu}$ as a Kronecker product of two 2×2 matrices, and individually inverting them:

$$E_{e\mu} = E_e \otimes E_\mu = \begin{pmatrix} \epsilon_{\mathrm{R}}^e & \epsilon_{\mathrm{F}}^e \\ 1 - \epsilon_{\mathrm{R}}^e & 1 - \epsilon_{\mathrm{F}}^e \end{pmatrix} \otimes \begin{pmatrix} \epsilon_{\mathrm{R}}^\mu & \epsilon_{\mathrm{F}}^\mu \\ 1 - \epsilon_{\mathrm{R}}^\mu & 1 - \epsilon_{\mathrm{F}}^\mu \end{pmatrix} \tag{5.9}$$

$$E_{e\mu}^{-1} = E_e^{-1} \otimes E_\mu^{-1} \tag{5.10}$$

$$= \frac{1}{\epsilon_{\mathrm{R}}^e - \epsilon_{\mathrm{F}}^e} \begin{pmatrix} 1 - \epsilon_{\mathrm{F}}^e & -\epsilon_{\mathrm{F}}^e \\ -1 + \epsilon_{\mathrm{R}}^e & \epsilon_{\mathrm{R}}^e \end{pmatrix} \otimes \frac{1}{\epsilon_{\mathrm{R}}^\mu - \epsilon_{\mathrm{F}}^\mu} \begin{pmatrix} 1 - \epsilon_{\mathrm{F}}^\mu & -\epsilon_{\mathrm{F}}^\mu \\ -1 + \epsilon_{\mathrm{R}}^\mu & \epsilon_{\mathrm{R}}^\mu \end{pmatrix} \tag{5.11}$$

Using this inverse, one arrives at coefficients to calculate the fake lepton contributions from N_{TT}, N_{TL}, N_{LT} and N_{LL}.

Since the resulting fake background estimate dependends linearly on the event counts, it can be implemented with event weights: Take all data events, apply the analysis cuts (depending on the region being analyzed) except for lepton isolation, and weight each event with the applicable coefficient depending on the isolation and momenta of the two leptons. These weights are plotted in figure 5.14. The count and distribution of the resulting samples represents the matrix method estimate of the background due to misidentified jets. [59]
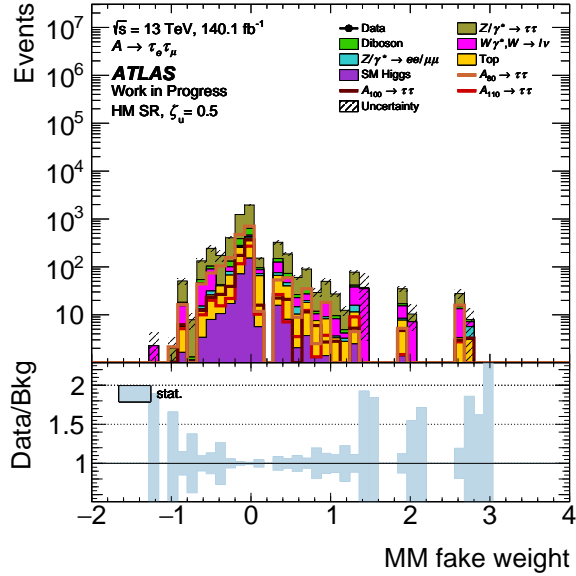

Figure 5.14: Distribution of weights used for the matrix method estimate, when applied to high-mass Signal Region backgrounds.

The calculation of the required weights is implemented in the `FakeBkgTool`, which is maintained by the ATLAS Isolation and Fake Forum (IFF) and is part of the ATLAS Athena software framework [60].

Unfortunately, this implementation can only be used during an early data processing step in our analysis, which makes it impossible to adjust the efficiencies without rerunning an unnecessarily large part of the code. Additionally, it only allows us to calculate the total background from fakes, not the individual contributions from events with a fake electron, with a fake muon and with two fake leptons. Splitting the contributions is useful to check plausibility and agreement with the single-lepton Monte Carlo backgrounds.

To avoid these issues, I implemented a Python module which calculates the weights for each background type separately, and can be used in a later analysis step. The total of all fake background estimates is consistent with the IFF `FakeBkgTool`.

5.6 Systematic uncertainties

It is only possible to calculate the statistical significance of a potential result when the sizes of all uncertainties are known. Therefore, the estimation of systematic uncertainties from all possible sources is an important part of the analysis.

The uncertainties are divided into *experimental uncertainties*, which are related to the experiment at the ATLAS detector and the subsequent reconstruction process, and *theoretical uncertainties*, which are due to our modeling of signal and background processes.

5.6.1 Experimental uncertainties

Since the experimental uncertainties are mostly the same across all analyses which use data from the ATLAS detector, they can be estimated centrally. For each physics object or reconstruction step, the responsible combined performance group usually publishes a set of variations to be applied. The variations are grouped by the source and type of the uncertainty they model:

- The electron calibration systematics (`EG`) cover the imperfect modeling of electron energy measurements. This includes variations of the energy resolution and scale.

- Electron efficiency variations (`EL_EFF`) are related to the probabilities with which an electron in the detector activates the trigger system, is correctly reconstructed, and passes the identification and isolation criteria. Uncertainties in the measurements of these efficiencies affect the simulated electron detection process.

- Analogously to the electron systematics, there is a variation group for muon calibration (`MUON`), which varies the parameters of the simulated muon momentum reconstruction algorithm, and for muon efficiencies (`MUON_EFF`).

- Even though this analysis uses a final state which does not include jets, it is influenced by jet calibration and efficiency uncertainties (`JET`) via b-tagging and the

missing transverse energy. The flavor tagging algorithm also has its own set of systematics (`FT_EFF`).

- Aside from reconstructed electron, muon and jet transverse momenta, the missing transverse energy also includes track-based soft terms which represent the momenta of partices which could not be reconstructed. Their scale and resolution uncertainties are covered by the missing transverse momentum variations (`MET`).

- Finally, the total luminosity of the recorded ATLAS data (`LUMI`) and the amount of pile-up inside the detector (`PRW_DATASF`) are also important parameters which have their own systematic uncertainties.

5.6.2 Theoretical cross-section uncertainties

To predict the rate of background events and the distributions of the particle momenta, it is necessary to know the production cross-sections of the different background resonances and to simulate their decays. Both the cross-section values and Monte Carlo simulations are affected by systematic uncertainties. The former are discussed in the following paragraphs, while the latter are examined in the next section.

For the background cross-sections of the $Z \to \tau\tau$ and Diboson processes, measured values from ATLAS data are used [61, 62]. Taking the stated uncertainties on these results into account leads to a 5% variation on Z boson decays and 7.1% on Diboson processes.

The cross-sections for $t\bar{t}$ processes were calculated perturbatively using `TOP++` [63]. The quadratic summation of scale, PDF and α_s variations gives a total uncertainty of 4.4%.

The uncertainty of the signal cross-section is of somewhat lower importance, since they do not affect the statistical significance of a given difference between background and data. Nonetheless, it is needed to calculate confidence intervals and exclusion limits for model parameters like ζ_u. The possible variance is dominated by the uncertainty due to higher orders omitted from the fixed-order perturbative calculation, and has a lower contribution from the uncertainty on the strong coupling constant α_s. The relative uncertainty ranges from 6.5% for $m_A = 110\,\mathrm{GeV}$ to 11.2% for $m_A = 20\,\mathrm{GeV}$.

5.6.3 Theoretical Monte Carlo modeling uncertainties

Due to the various approximations and phenomenological values used in Monte Carlo simulations, they are strongly affected by systematic uncertainties. They are estimated according to the recommendations of the ATLAS Physics Modeling Group. The estimation procedure for the background from top quark pairs is explained in detail in the following paragraphs.

The most significant systematic is due to the scale-dependent procedures for renormalization and factorization applied during the calculation of the initial-state radiation (ISR). Their combined uncertainty is estimated using a *7-point variation*. Starting from the nominal sample, the values of the renormalization scale μ_R and factorization scale

μ_F are independently varied by a factor of 0.5 and 2, and additionally both scales are simultaneously varied by the same factor. The 7 resulting combinations are listed in table 5.3. From these variations, the minimum and maximum is used at every parameter value.

Variation	μ_R	μ_F
#1	1	1
#2	0.5	1
#3	2	1
#4	1	0.5
#5	1	2
#6	0.5	0.5
#7	2	2

Table 5.3: Variation factors for the renormalization and factorization scales used in a 7-point variation.

To take the dependence on the parton density functions into account, the 100 variations contained in the `NNLPDF30` PDF set are used. Their standard deviation represents the PDF uncertainty estimate.

The strong coupling constant α_S affects the result via its effect on the initial state radiation, but also via an α_S-dependence of the PDF. The Monte Carlo generator and PDF set both provide up- and down-variations for this application.

The POWHEG method used for the matching between NLO matrix elements and parton shower is parameterized by the resummation damping factor h_{damp}. The nominal sample is generated with $h_{damp} = 1.5 m_{top}$, and an alternative sample using a value of $3 m_{top}$ is used to estimate the uncertainty due to the resummation procedure. A variation in the other direction is not available, so the difference to the nominal sample is taken as the absolute uncertainty in both directions.

Other uncertainties are due to specific assumptions used in the Monte Carlo generator code. These are not as easily evaluated through parameter variations and are instead estimated by using alternative samples produced with other generator programs. The nominal top quark background is generated using a combination of `Pythia 8` to simulate parton shower and hadronization together with `POWHEG-BOX v2` to calculate the next-to-leading order matrix elements and their matching to the parton shower. Therefore, it is possible to get separate estimates for the impacts of parton shower and matrix element by switching out each part of the generator separately. The `Herwig 7` parton shower generator is used as an alternative to `Pythia`, and the matrix element generator `MadGraph5_aMC@NLO` is used in place of `POWHEG-BOX`.

To keep the influence of low Monte Carlo sample statistics on the systematic uncertainty estimate down, the relative size of each systematic variation is calculated in the Top Validation Region as a function of the main mass variable m_{MMC} and afterwards applied to the Top background in every region. This is possible because the TVR only

differs from the SR in the b-tag requirement and is therefore kinematically very close, and so the effect of each variation on the Top background should be the same in TVR and SR. The calculated uncertainty sizes are shown in figure 5.15.
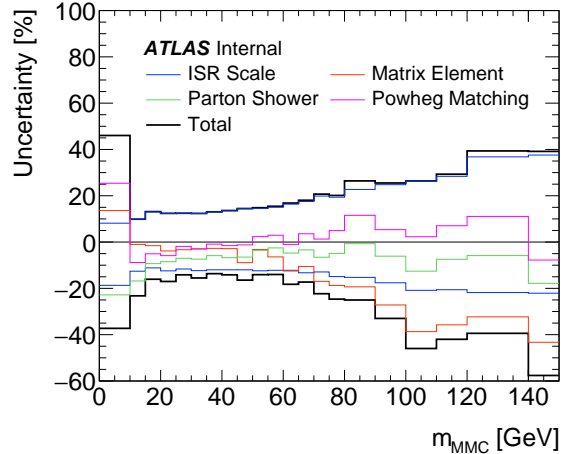

Figure 5.15: Total relative theoretical uncertainty for top quark processes binned in m_{MMC}, together with the four largest contributions. They are measured using data from the Top Validation Region

The largest influence on average is due to the scale variation in ISR. This is not surprising, since it quantifies the influence of the two major approximations used for QFT calculations. The first is fixed order perturbation theory which neglects all higher orders, i.e. terms which include higher powers of the coupling constants, and is used for the matrix element of the hard process. The matrix element generator used for top quark samples only calculates the leading and next-to-leading order (NLO) contributions. The second is parton shower factorization, which leaves out quantum interference terms between the factors. These approximations are necessary to keep the problem algorithmically tractable, but also introduce significant systematic uncertainties.

The parton shower and matrix element variations which switch out the respective parts of the generator setup are also significant. This represents the difference in the calculation schemes and phenomenological models: In the case of the parton shower generator, it might be the different hadronization and decay models, while for the matrix element generator, it likely comes from the different matching schemes (POWHEG and aMC@NLO) which prevent double-counting of terms between fixed-order and shower calculations.

Uncertainties on the $Z \rightarrow \tau\tau$ and Diboson backgrounds are estimated using a similar process as for $t\bar{t}$ and are plotted in figures 5.16 and 5.17.

The QCD scale uncertainties are derived from the previously discussed 7-point variation of the renormalization and factorization scales. The PDF uncertainty is taken as the standard deviation within the NNLPDF30 PDF set. Since the weak boson decay
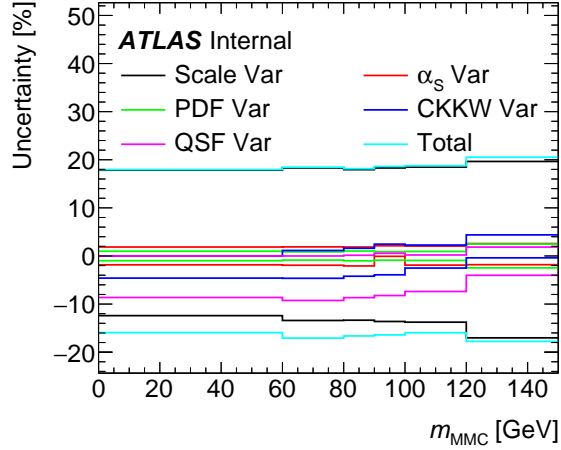
Figure 5.16: Total relative theoretical uncertainty for the $Z \rightarrow \tau\tau$ process binned in m_{MMC}, together with different contributions.

samples are produced with SHERPA, they use QSF resummation and CKKW matching instead of POWHEG. The uncertainty in the QSF method is estimated by varying the resummation scale μ_{QSF} by a factor of 0.5 and 2, and the CKKW uncertainty is deduced by varying its overlap scale parameter by a factor of 0.75 and 1.5. For Diboson events, QSF and CKKW systematics are set to zero since the required variation samples are not available and the uncertainties are expected to be negligible on the relatively small Diboson background contribution.
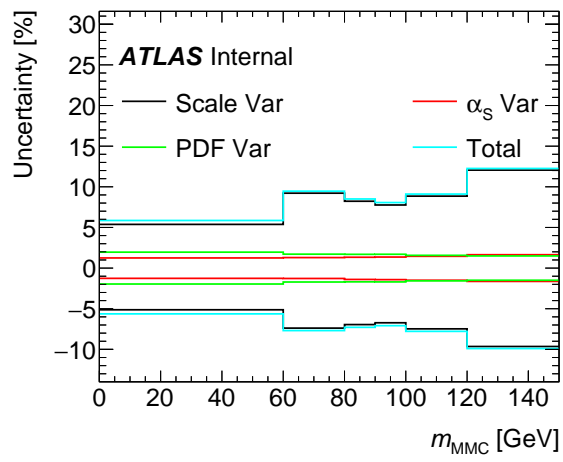
Figure 5.17: Total relative theoretical uncertainty for Diboson processes binned in m_{MMC}, together with different contributions.

6 Results

The analysis is still blinded, so no results based on experimental data can be presented here. Instead, expected values for the exclusion limits are calculated. They are based on the assumption that the data follows the distribution predicted by the Standard Model, and delineate the region in which the analysis is sensible to a possible signal.

The limits are set on the rate of the signal process, expressed as the product of the $gg \rightarrow A$ production cross section and the brancing ratio of the decay $A \rightarrow \tau\tau$ with both tau leptons further decaying leptonically. The expected limit on this quantity $\sigma(gg \rightarrow A) \times B(A \rightarrow \tau_{\text{lep}}\tau_{\text{lep}})$ varies between $0.5\,\text{pb}$ and $3.8\,\text{pb}$, as shown in figure 6.1. This limit is obtained using the `WSMaker` tool [64], which analyses the shape of the m_{MMC} distribution in the signal region and takes the overlap between the signals for different mass hypotheses into account.
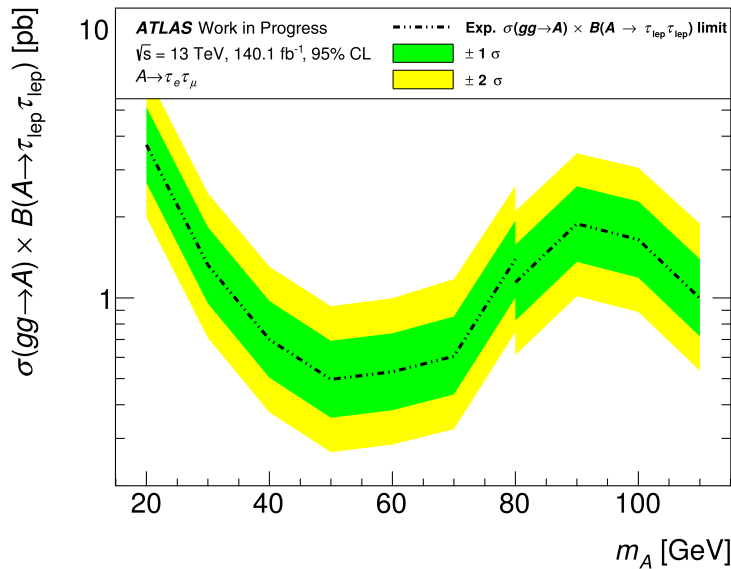

Figure 6.1: Expected upper limit on the product of product of the $gg \rightarrow A$ production cross section and the brancing ratio of A boson decay into two leptonically decaying tauons for A boson mass hypotheses from $20\,\text{GeV}$ to $110\,\text{GeV}$.

The strongest limit is obtained for $m_A = 50\,\text{GeV}$. Towards lower A boson masses, a smaller percentage of signal events pass the trigger thresholds and selection criteria, and around $90\,\text{GeV}$, the signal-to-noise ratio deteriorates due to the high $Z \rightarrow \tau\tau$ background. The discontinuity at $m_A = 80\,\text{GeV}$ corresponds to the switch between the low-mass and

high-mass signal region cuts.

The cross-section limits can be translated into limits on the up-type quark coupling parameter ζ_u, since the theoretical 2HDM prediction of the A boson production cross-section is proportional to ζ_u^2. Taking the calculated value of the proportionality constant and its uncertainty into account, one obtains the upper limits on $|\zeta_u|$ as plotted in figure 6.2. The limits are expected to be below the previous constraint of about 0.5 across the whole mass range. The expected limits are especially low ($|\zeta_u| < 0.12$) between 20 GeV and 70 GeV, which is the most promising range for the 2HDM to explain the anomalous magnetic moment of the muon.
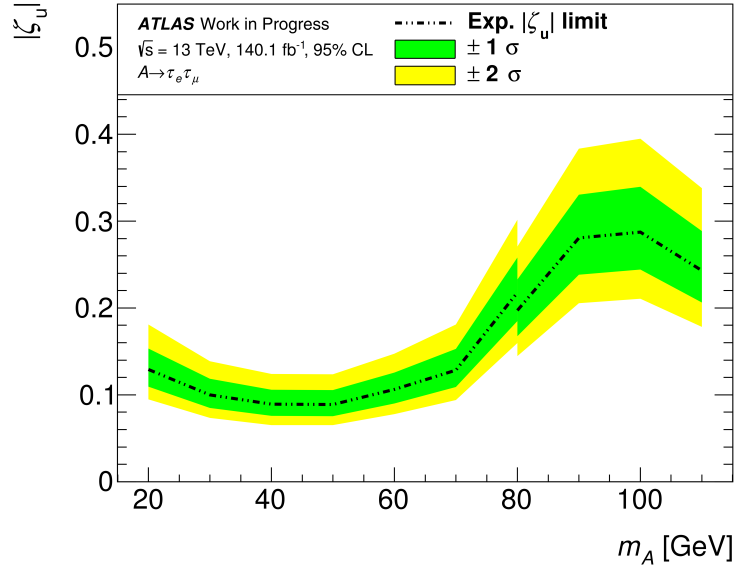

Figure 6.2: Expected upper limit on the absolute value of the up-type quark coupling parameter $|\zeta_u|$ for A boson mass hypotheses from 20 GeV to 110 GeV.

7 Summary and Outlook

In this thesis, an overview and new contributions to the search for a CP-odd Higgs boson with mass below $110\,\mathrm{GeV}$ have been presented. The existence of this CP-odd boson A is predicted by the two-Higgs doublet model (2HDM). The flavor-aligned 2HDM is an exciting candidate for physics beyond the Standard Model (SM), since it might explain the deviation between experimental measurements and SM predictions of the anomalous magnetic moment of the muon.

The analysis uses data collected at the ATLAS detector during Run 2 of the LHC, which is derived from proton-proton collisions with a center-of-mass energy of $13\,\mathrm{TeV}$ and an integrated luminosity of $140\,\mathrm{fb}^{-1}$.

The signal process consists of the production of the A boson from gluon-gluon fusion via a top quark loop and its decay into a pair of tau leptons, which further decay into one electron and one muon together with four neutrinos. The largest backgrounds are due to Z bosons in the process $Z \to \tau\tau$, top quark pairs and weak boson pairs.

The analysis is especially sensitive in the region of 2HDM parameter space with small A boson mass $M_A \lesssim 80\,\mathrm{GeV}$ and large up-type quark coupling parameter $|\zeta_\mathrm{u}|$. This domain is especially promising for new discoveries since the contributions of the second Higgs doublet to the anomalous magnetic moment of the muon are higher there. The expected limits on $|\zeta_\mathrm{u}|$ reach down to 0.1, above which a discovery would be possible.

The analysis was previously missing an estimate of the theoretical background uncertainties due to the use of Monte Carlo generated samples. They represent a significant contribution to the total uncertainty, so it is important to take them into account.

Due to concerns about the previously used approach, the matrix method was implemented to calculate an estimate of the background due to fake leptons mainly caused by misidentified jets. The new implementation can separately estimate the contributions from Multijet processes and both types of single-lepton fake events, only using the data and separately calculated efficiencies.

With the discussed improvements, the analysis is headed towards unblinding, which will finally allow a calculation of significances, favored parameter values and/or experimental limits. It is currently undergoing review by the ATLAS Higgs and Diboson Searches (HDBS) editorial board.

Since the start of Run 3 of the LHC, new data is being recorded by ATLAS. Due to improved detector, trigger and readout systems as well as a higher luminosity, a much more powerful search for evidence of the 2HDM will most likely be possible with a new analysis based on this data.

Bibliography

[1] J. J. Thomson, "Cathode rays", Phil. Mag. Ser. 5 **44**, 293–316 (1897).

[2] S. Tomonaga, "On a relativistically invariant formulation of the quantum theory of wave fields", Prog. Theor. Phys. **1**, 27–42 (1946).

[3] J. S. Schwinger, "Quantum electrodynamics. I A covariant formulation", Phys. Rev. **74**, edited by K. A. Milton, 1439 (1948).

[4] Y. Ne'eman, "Derivation of strong interactions from a gauge invariance", Nucl. Phys. **26**, edited by R. Ruffini and Y. Verbin, 222–229 (1961).

[5] M. Gell-Mann, "The Eightfold Way: A Theory of strong interaction symmetry", `10.2172/4008239` (1961).

[6] G. Zweig, "An SU(3) model for strong interaction symmetry and its breaking. Version 2", in *DEVELOPMENTS IN THE QUARK THEORY OF HADRONS. VOL. 1. 1964 - 1978*, edited by D. B. Lichtenberg and S. P. Rosen (Feb. 1964), pp. 22–101.

[7] M. Gell-Mann, "A Schematic Model of Baryons and Mesons", Phys. Lett. **8**, 214–215 (1964).

[8] S. Weinberg, "Nonabelian Gauge Theories of the Strong Interactions", Phys. Rev. Lett. **31**, 494–497 (1973).

[9] H. Fritzsch, M. Gell-Mann, and H. Leutwyler, "Advantages of the Color Octet Gluon Picture", Phys. Lett. B **47**, 365–368 (1973).

[10] S. L. Glashow, "Partial Symmetries of Weak Interactions", Nucl. Phys. **22**, 579–588 (1961).

[11] A. Salam, "Renormalizability of gauge theories", Phys. Rev. **127**, 331–334 (1962).

[12] P. W. Higgs, "Broken Symmetries and the Masses of Gauge Bosons", Phys. Rev. Lett. **13**, edited by J. C. Taylor, 508–509 (1964).

[13] F. Englert and R. Brout, "Broken Symmetry and the Mass of Gauge Vector Mesons", Phys. Rev. Lett. **13**, edited by J. C. Taylor, 321–323 (1964).

[14] G. S. Guralnik, C. R. Hagen, and T. W. B. Kibble, "Global Conservation Laws and Massless Particles", Phys. Rev. Lett. **13**, edited by J. C. Taylor, 585–587 (1964).

[15] T. W. B. Kibble, "Symmetry breaking in nonAbelian gauge theories", Phys. Rev. **155**, edited by J. C. Taylor, 1554–1561 (1967).

[16] G. Arnison et al. (UA1), "Experimental Observation of Lepton Pairs of Invariant Mass Around 95-GeV/c**2 at the CERN SPS Collider", Phys. Lett. B **126**, 398–410 (1983).

[17] M. Banner et al. (UA2), "Observation of Single Isolated Electrons of High Transverse Momentum in Events with Missing Transverse Energy at the CERN anti-p p Collider", Phys. Lett. B **122**, 476–485 (1983).

[18] G. Aad et al. (ATLAS), "Observation of a new particle in the search for the Standard Model Higgs boson with the ATLAS detector at the LHC", Phys. Lett. B **716**, 1–29 (2012).

[19] S. Chatrchyan et al. (CMS), "Observation of a New Boson at a Mass of 125 GeV with the CMS Experiment at the LHC", Phys. Lett. B **716**, 30–61 (2012).

[20] A. Einstein, "The Field Equations of Gravitation", Sitzungsber. Preuss. Akad. Wiss. Berlin (Math. Phys.) **1915**, 844–847 (1915).

[21] P. Moder, "Search for a light CP-odd Higgs boson decaying into a $\tau\tau$ pair", MA thesis (TU Dresden, Germany, 2018).

[22] T. Kreße, "Search for a light CP-odd Higgs boson decaying into a pair of τ-leptons with the ATLAS detector", MA thesis (TU Dresden, Germany, 2020).

[23] X.-M. Sonntag, "Optimized search for a light CP-odd Higgs boson decaying into a two τ-leptons using the ATLAS detector", MA thesis (TU Dresden, Germany, 2021).

[24] J. Ellis, "Higgs Physics", 2013 European School of High-Energy Physics, 117–168 (2015).

[25] G. Feinberg and S. Weinberg, "On the phase factors in inversions", Il Nuovo Cimento (1955-1965) **14**, 571–592 (1959).

[26] G. Luders, "Proof of the TCP theorem", Annals Phys. **2**, 1–15 (1957).

[27] L. Fromme, S. J. Huber, and M. Seniuch, "Baryogenesis in the two-Higgs doublet model", JHEP **11**, 038 (2006).

[28] K. Enomoto, S. Kanemura, and Y. Mura, "Electroweak baryogenesis in aligned two Higgs doublet models", JHEP **01**, 104 (2022).

[29] H. Haber and G. Kane, "The search for supersymmetry: probing physics beyond the standard model", Physics Reports **117**, 75–263 (1985).

[30] G. C. Branco, P. M. Ferreira, L. Lavoura, M. N. Rebelo, M. Sher, and J. P. Silva, "Theory and phenomenology of two-Higgs-doublet models", Phys. Rept. **516**, 1–102 (2012).

[31] A. Cherchiglia, D. Stöckinger, and H. Stöckinger-Kim, "Muon g-2 in the 2HDM: maximum results and detailed phenomenology", Phys. Rev. D **98**, 035001 (2018).

[32] E. A. Paschos, "Diagonal Neutral Currents", Phys. Rev. D **15**, 1966 (1977).

[33] A. Pich and P. Tuzon, "Yukawa Alignment in the Two-Higgs-Doublet Model", Phys. Rev. D **80**, 091702 (2009).

[34] P. Athron, C. Balázs, D. H. J. Jacob, W. Kotlarski, D. Stöckinger, and H. Stöckinger-Kim, "New physics explanations of a_μ in light of the FNAL muon g − 2 measurement", JHEP **09**, 080 (2021).

[35] G. W. Bennett et al. (Muon g-2), "Final Report of the Muon E821 Anomalous Magnetic Moment Measurement at BNL", Phys. Rev. D **73**, 072003 (2006).

[36] B. Abi et al. (Muon g-2), "Measurement of the Positive Muon Anomalous Magnetic Moment to 0.46 ppm", Phys. Rev. Lett. **126**, 141801 (2021).

[37] V. Ilisie, "New Barr-Zee contributions to $(\mathbf{g} - \mathbf{2})_\mu$ in two-Higgs-doublet models", JHEP **04**, 077 (2015).

[38] A. Cherchiglia, P. Kneschke, D. Stöckinger, and H. Stöckinger-Kim, "The muon magnetic moment in the 2HDM: complete two-loop result", JHEP **01**, 007 (2017).

[39] L. Evans and P. Bryant, "Lhc machine", Journal of Instrumentation **3**, S08001 (2008).

[40] E. Lopienska, "The CERN accelerator complex, layout in 2022", (2022).

[41] G. Aad et al. (ATLAS), "The ATLAS Experiment at the CERN Large Hadron Collider", JINST **3**, S08003 (2008).

[42] S. Chatrchyan et al. (CMS), "The CMS Experiment at the CERN LHC", JINST **3**, S08004 (2008).

[43] K. Aamodt et al. (ALICE), "The ALICE experiment at the CERN LHC", JINST **3**, S08002 (2008).

[44] A. A. Alves Jr. et al. (LHCb), "The LHCb Detector at the LHC", JINST **3**, S08005 (2008).

[45] J. Wenninger, "Operation and Configuration of the LHC in Run 2", (2019).

[46] ATLAS Collaboration, "Luminosity determination in pp collisions at $\sqrt{s} = 13$ TeV using the ATLAS detector at the LHC", (2022).

[47] E. Torrence et al. (ATLAS), *Public ATLAS Luminosity Results for Run-2 of the LHC*, `https://twiki.cern.ch/twiki/bin/view/AtlasPublic/LuminosityPubli cResultsRun2`, [Accessed 2023-06-01; Available at Internet Archive].

[48] S. Fartoukh et al., *LHC Configuration and Operational Scenario for Run 3*, tech. rep. (CERN, Geneva, 2021).

[49] B. Abbott et al. (ATLAS IBL), "Production and Integration of the ATLAS Insertable B-Layer", JINST **13**, T05008 (2018).

[50] F. Siegert, "Monte-Carlo event generation for the LHC", PhD thesis (Durham U., 2010).

[51] A. Buckley, J. Ferrando, S. Lloyd, K. Nordström, B. Page, M. Rüfenacht, M. Schönherr, and G. Watt, "LHAPDF6: parton density access in the LHC precision era", Eur. Phys. J. C **75**, 132 (2015).

[52] E. Bothmann et al. (Sherpa), "Event Generation with Sherpa 2.2", SciPost Phys. **7**, 034 (2019).

[53] T. Sjöstrand, S. Ask, J. R. Christiansen, R. Corke, N. Desai, P. Ilten, S. Mrenna, S. Prestel, C. O. Rasmussen, and P. Z. Skands, "An introduction to PYTHIA 8.2", Comput. Phys. Commun. **191**, 159–177 (2015).

[54] C. Oleari, "The POWHEG-BOX", Nucl. Phys. B Proc. Suppl. **205-206**, edited by J. Blümlein, S.-O. Moch, and T. Riemann, 36–41 (2010).

[55] J. Alwall, R. Frederix, S. Frixione, V. Hirschi, F. Maltoni, O. Mattelaer, H. .-. Shao, T. Stelzer, P. Torrielli, and M. Zaro, "The automated computation of tree-level and next-to-leading order differential cross sections, and their matching to parton shower simulations", JHEP **07**, 079 (2014).

[56] J. Bellm et al., "Herwig 7.0/Herwig++ 3.0 release note", Eur. Phys. J. C **76**, 196 (2016).

[57] R. L. Workman et al. (Particle Data Group), "Review of Particle Physics", PTEP **2022**, 083C01 (2022).

[58] *Identification of Jets Containing b-Hadrons with Recurrent Neural Networks at the ATLAS Experiment*, tech. rep. (CERN, Geneva, 2017).

[59] ATLAS Collaboration, *Tools for estimating fake/non-prompt lepton backgrounds with the ATLAS detector at the LHC*, tech. rep. (Geneva, Nov. 2022).

[60] ATLAS Collaboration, "Athena", `10.5281/zenodo.4772550` (2021).

[61] G. Aad et al. (ATLAS), "Measurement of $W^{\pm}$ and Z-boson production cross sections in pp collisions at $\sqrt{s} = 13$ TeV with the ATLAS detector", Phys. Lett. B **759**, 601–621 (2016).

[62] M. Cristinziani (ATLAS), "Recent diboson and multiboson results in ATLAS", PoS **LHCP2019**, edited by P. Roig Garcés, I. Bautista Guzman, A. Fernández Téllez, and M. I. Martínez Hernández, 157 (2019).

[63] M. Czakon and A. Mitov, "Top++: A Program for the Calculation of the Top-Pair Cross-Section at Hadron Colliders", Comput. Phys. Commun. **185**, 2930 (2014).

[64] N. Morange et al. (ATLAS Higgs Working Group), *WorkspaceMaker*, `https://t wiki.cern.ch/twiki/bin/view/AtlasProtected/WorkspaceMaker`, (ATLAS Internal).

Erklärung

Hiermit erkläre ich, dass ich diese Arbeit im Rahmen der Betreuung am Institut
für Kern- und Teilchenphysik ohne unzulæssige Hilfe Dritter verfasst und alle
Quellen als solche gekennzeichnet habe.

Christian Schmidt
Dresden, 15.06.2023